Journal of The Electrochemical Society



OPEN ACCESS

# PEM Single Cells under Differential Conditions: Full Factorial Parameterization of the ORR and HOR Kinetics and Loss Analysis

To cite this article: Christophe Gerling *et al* 2022 *J. Electrochem. Soc.* **169** 014503

*Journal of The Electrochemical Society*, 2022 **169** 014503

# PEM Single Cells under Differential Conditions: Full Factorial Parameterization of the ORR and HOR Kinetics and Loss Analysis

**Christophe Gerling,[1,2,z] Matthias Hanauer,[1] Ulrich Berner,[1] and K. Andreas Friedrich[2,3]**

[1]*Robert Bosch GmbH, Corporate Research, Robert-Bosch-Campus 1, Renningen 71272, Germany*
[2]*Institute for Building Energetics, Thermotechnology and Energy Storage (IGTE), University of Stuttgart, Pfaffenwaldring 6, Stuttgart 70569, Germany*
[3]*Institute of Engineering Thermodynamics, German Aerospace Center (DLR), Pfaffenwaldring 38-40, Stuttgart 70569, Germany*

The anode and cathode kinetics are parameterized based on differential cell measurements. Systematic parameter variations are evaluated to disentangle the dependencies of the electrochemical impedance spectroscopy (EIS) signatures in $H_2/H_2$ mode. We introduce a new CO recovery protocol for both electrodes that enables to accurately characterize the hydrogen oxidation reaction (HOR) kinetics. Then, we demonstrate that a compact Tafel kinetics law captures the oxygen reduction reaction (ORR) kinetics for a full factorial grid of conditions, covering a wide range of relative humidities (*rH*), temperatures, oxygen partial pressures and current densities. This yields the characteristic activation energy and effective reaction order, and we reconcile models that make different assumptions regarding the *rH* dependency. Moreover, we analyze $O_2$ transport contributions by steady-state and transient limiting current techniques and heliox measurements. Although the rising uncertainty of loss corrections at high current densities makes it impossible to unambiguously identify an intrinsic potential-dependent change of the Tafel slope, our data support that such effect needs not be considered for steady-state cathodic half-cell potentials above 0.8 V.

 [DOI: 10.1149/1945-7111/ac44ba]

Manuscript submitted September 20, 2021; revised manuscript received December 9, 2021. Published January 5, 2022.

Supplementary material for this article is available online

As of today, the lifetime and costs of PEM fuel cells are still the most important barriers to a wide commercialization. Within the cost, the membrane electrode assemblies (MEA) represent up to 50% of the total expenses (40% for the electrodes alone).[1] Thus, one way of optimization lies in enhancing the MEAs which requires understanding the influence of the operating parameters on the performance. The most important physicochemical processes limiting the performance are the cathode and anode kinetics, the Ohmic contribution, and finally the species transport from the gas channel to the triple phase boundaries (TPB).[2–4] This leads to a polarization curve described by

$$U_{\text{cell}} = U_0 - \eta_{\text{ORR}} - \eta_{\text{HOR}} - \eta_{\text{MT}} - j\cdot(R_\Omega + R_{\text{p}}^{\text{eff}}) \qquad [1]$$

with $U_0$ the equilibrium cell voltage, $\eta_{\text{ORR}}$ and $\eta_{\text{HOR}}$ the overpotential of the cathode and anode kinetics (ORR for oxygen reduction reaction and HOR for hydrogen oxidation reaction), and $\eta_{\text{MT}}$ the voltage drop due to mass transport contributions. The Ohmic contribution from $(R_\Omega + R_{\text{p}}^{\text{eff}})$ is proportional to the current density and contains proton transport in the polymer electrolyte membrane (PEM) and the catalyst layers (CL), electron transport and all the contact resistances. Even though these mechanisms are strongly overlapping in full cell configurations, they are generally addressed separately in the literature, making it difficult to find consistent parameter sets for given material combinations. Moreover, different measurement setups or techniques often lead to discrepancies in the results, which is shown in the scatter in the available data,[5] and material parameterizations become increasingly outdated, as recently discussed by Dickinson and Smith for membrane properties.[6] For these reasons, there is a need for fast in situ characterization workflows to parameterize state-of-the-art materials. We started to address this need in our previous publication concerning the parameterization of the hydrogen permeation and the ionomer conductivities in a full factorial manner, where we also investigated the changes in these properties under load due to the product water.[7]

In this work, we continue our investigations with a special focus on the parameterization of the ORR and HOR based on the most comprehensive dataset in the literature to our knowledge. Polarization data and electrochemical impedance spectroscopy (EIS) were recorded for over 1400 operating conditions (see Fig. 1 and detailed description of the test run below).

Albeit the hydrogen sorption and reaction kinetics on platinum and alloy catalysts have been widely studied, the HOR is often neglected in full cell studies for the sake of simplicity, justified by the high rates of the kinetics. Nevertheless, the anode is usually low-loaded with platinum and thus the HOR overpotential is not necessarily negligible. So far, in full cells and gas diffusion electrodes in three-electrode setups, the HOR has mainly been studied by voltammetry and polarization techniques,[8–14] or by EIS. The EIS response of an $H_2/H_2$ cell generally exhibits two capacitive semicircles: the high frequency (HF) loop that is usually assigned to the charge transfer and proton conduction within the catalyst layer,[9,15–17] and the low frequency (LF) loop that is sometimes assigned to hydrogen chemisorption (independent of the partial pressure).[15,16] In contradiction with these findings and based on proton pumping measurements under load with only nitrogen on the cathode side, Huth et al. argued that the HF loop represents the anodic oxidation of hydrogen and the LF loop the reduction of protons to $H_2$ on the cathode side.[10] Also, Heinzmann et al. identified three processes in their $H_2/H_2$ measurements with symmetrical electrodes using the distribution of relaxation times (DRT), all three being strongly dependent on the hydrogen partial pressure.[18] In this work, we show an extensive characterization of the performance of our MEA under $H_2/H_2$ conditions with EIS at open circuit voltage (OCV) and polarization data. Therein, we vary the relative humidity *rH*, the temperature *T* and the hydrogen partial pressure $p_{H_2}$ individually. Additionally, we introduce an effective recovery technique to oxidize parasitic CO within both electrodes almost simultaneously that allows us to access the kinetics without influence of surface poisoning. This permits us to discuss in detail the performance signatures of the proton pump operation mode and the correction for the anode contributions under fuel cell ($H_2/O_2$) mode.

Among the loss mechanisms, the sluggish oxygen reduction reaction (ORR) on the cathode side still represents the most

[z]E-mail: christophe.gerling@de.bosch.com

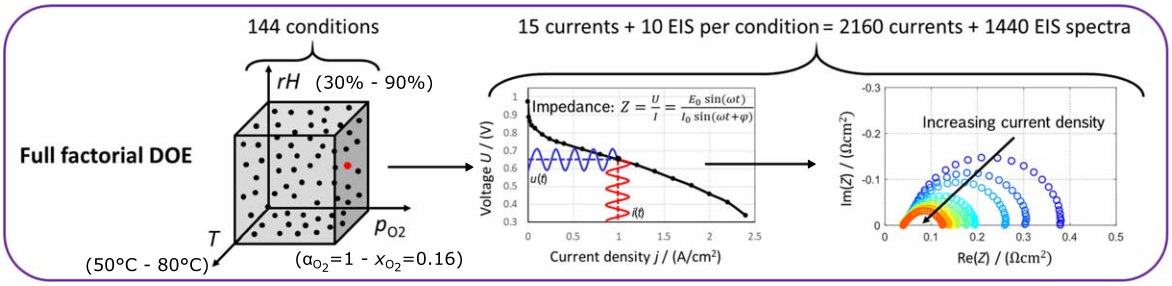


**Figure 1.** Schematic of our full factorial design of experiments in fuel cell mode. For each condition, polarization (16 currents) and EIS (10 currents) data were recorded.

important contribution to the overpotential under system relevant operating conditions. However, even though the ORR has been widely studied in the literature, it is still subject to research activities and there is no consensus concerning its modeling and parameterization yet. We aim at addressing these issues by meticulously analyzing our extensive dataset. This is challenging nonetheless since several loss mechanisms overlap in a full cell setup, making it difficult to properly extract pure ORR kinetics over a wide range of current densities. In the most simple approach, the ORR is described by Tafel kinetics with one intrinsic slope given by $-\ln(10)RT/(\alpha F)$, where $\alpha \approx 1$.[19] This is equivalent to 60–70 mV/dec at typical fuel cell operation temperatures. However, rotating disc electrode (RDE) and microelectrode measurements showed that $\alpha$ can decrease to 0.5 at potentials below 0.8 V, confirmed by different modeling studies.[20–22] This change in the slope has been explained by more complex ORR kinetics including changes in the platinum surface coverage and potential-dependent changes of the rate limiting step and various descriptions were integrated in physical models of full cells.[23–26] Despite the difficulty to capture this effect in full cell measurements (the *jR*-corrected voltages are usually higher than 750 mV with loadings $> 0.2\ \mathrm{mg_{Pt}\ cm^{-2}_{geo}}$), Subramanian et al. were able to parameterize a coverage-dependent model that was in agreement with their data by using an MEA with a low-loaded cathode.[27] Besides these effects, it is known that the proton conduction within the electrodes of full cells can also lead to a doubling of the apparent Tafel slope in the high current regime.[3,28] The analyses in full cells are therefore usually carried out for low current densities with pure $O_2$ at $rH = 100\%$ and the data are corrected by the protonic loss contributions $j\cdot(R_\Omega + R_p^{\mathrm{eff}})$. This

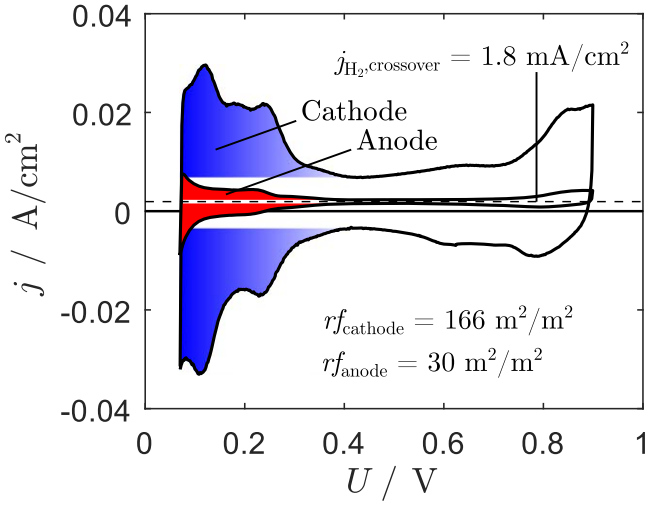


**Figure 2.** CV of the cathode (blue) and the anode (red) at $rH$=100 %, $T = 40$ °C and $p_{\mathrm{total}} = 1.0\ \mathrm{bar_a}$, recorded with a sweep rate of 100 mV $\mathrm{s^{-1}}$ from 70 mV to 900 mV. The extracted roughness factors *rf* and the $H_2$ crossover current $j_{H_2,\mathrm{crossover}}$ are also shown.

enables to guarantee a homogeneous distribution of the ORR within the CCL and to limit mass transport issues. In this work, we will also cover such conditions and present a full factorial parameterization of the ORR based on a simple Tafel law. The necessity of a more sophisticated ORR model will also be discussed. We will further investigate the influence of the relative humidity on the ORR by comparing a $p_{H_2O}$-dependent and a $p_{H_2O}$-independent model.

For estimating the $O_2$ mass transport contribution to the overall performance loss, the low frequency signatures of the cell impedance can be investigated.[18,29] To do this, several methods have been used in the literature, including fitting simple Randles circuits or transmission line models (TLM) containing a mass transport element (often Warburg) either in series with the charge transfer resistance[30–32] or with the whole circuit,[33–36] or fitting more sophisticated physical models exhibiting analytical solutions under specific assumptions.[37] However, the low frequency domain might also contain other mechanisms that overlap frequency-wise (slow water management contributions for instance), making the analysis challenging. Another technique is the limiting current measurement, where low $O_2$ concentrations are usually used in order to analyze the transport resistance.[38] Although the measurement principle is straightforward, limiting current data requires careful analysis because $O_2$ mass transport strongly depends on the CCL and GDL water household. This can manifest itself as a steady increase of the mass transport resistance in course of rising $O_2$ concentration and hence rising limiting current density and water production,[39] which may result in the overestimation of mass transport induced voltage drops for lower current densities. An evaluation of how the transport resistance evolves in operation was only done recently by transient limiting current experiments.[40] We will use both limiting current techniques in this work to discuss the influence of oxygen transport on the performance.

In summary, the main goal of this work is to systematically extend our previously published full factorial in situ characterization approach[7] to disentangle further loss contributions. We thus aim at proposing a seamless parameterization chain based on in situ techniques that can be applied to a material combination of choice. In this paper we will show the parameterization of ready-to-use models for the HOR and ORR with the relative humidity, the temperature and the partial pressures as parameters. Our findings will also be compared to results from the literature. Finally, we will discuss the mass transport contributions and perform a global loss analysis.

## Experimental

***Setup.***—In this work we used 12 $\mathrm{cm^2}$ Gore® PRIMEA® MEAs (W.L. Gore & Associates, Elkton, MD, USA) with a membrane thickness of 18 $\mu$m and platinum loadings of 0.4 $\mathrm{mg_{Pt}\ cm^{-2}}$ in the cathode and 0.05 $\mathrm{mg_{Pt}\ cm^{-2}}$ in the anode. Figure 2 superposes typical cathode and anode voltammograms for such an MEA. The roughness factors *rf* were calculated by integrating the colored $H_{UPD}$ areas and averaging over the adsorption and desorption processes (see also Fig. S1 of the supplementary material, available at stacks.iop.org/JES/169/014503/mmedia). The results were $rf_{\mathrm{cathode}} = 166 \pm 11\ \mathrm{m^2_{Pt}\ m^{-2}_{geo}}$ and

$rf_{anode} = 30 \pm 3\ m^2_{Pt}\ m^{-2}_{geo}$, determined over at least 10 CVs of each electrode.

The 12 $cm^2$ MEAs were laminated into polyethylene naphthalate frames at about 100 °C. The MEAs were sandwiched between Sigracet® 22BB gas diffusion layers (GDL) from SGL® Carbon and mounted in a differential cell setup from Baltic FuelCells (quickConnect®) with straight graphite flow fields. The equivalent clamping pressure on the active area was about 1.3 MPa.

For all our tests we employ a fully automated FuelCon Evaluator C50 test station. The cell temperature is measured by a type K thermocouple and regulated by a Huber Ministat 125 thermostat. For the EIS measurements, a Gamry reference 3000 plus Booster 30 K device in combination with the test station load were used and high precision was ensured by using a four-point measurement setup. More information about our setup is given in our previous publication.[7]

***Design of experiments and techniques.***—Our full factorial test run was carried out in four stages:

1. Cell conditioning.
2. Proton pump ($H_2/H_2$) and blocking cathode ($H_2/N_2$) experiments including CV and EIS measurements.
3. Fuel cell ($H_2/O_2$) experiments including polarization curves and EIS. Second separate run with heliox ($O_2$ and He mixtures in the cathode).
4. Separate test run in $H_2/O_2$ mode for limiting current measurements.

The conditioning was done in the $H_2$/air mode at $p_{total} = 1.5\ bar_a$, $rH = 100\%$, $T = 50$ °C, and with $H_2$/air flows of 1300/2000 sccm, according to the procedure described by Harzer et al.:[41] 0.6 V during 45 min, OCV during 5 min, and 0.85 V during 10 min. The cell performance was stable after repeating this ten times ( $\approx 10$ h) and then operating the cell at 0.3 V for 2 h.

The proton pump and blocking cathode measurements allowed us to characterize the proton conductivities, the hydrogen permeation coefficient and also the anode resistance in a full factorial manner under system relevant conditions. We varied the operating conditions from $rH = 30\%$ to $rH = 100\%$ and $T = 50$ °C to $T = 80$ °C at $p_{total} = 1.5\ bar_a$, leading to 32 operating conditions. For each of these conditions, EIS and CVs were recorded in $H_2/N_2$ mode and EIS and polarization curves in $H_2/H_2$ mode. The sequence was as follows for each humidity/temperature condition:

1. Setting the temperature and the dew point (from low to high dew points) in $H_2/N_2$ mode and letting the cell equilibrate for 2 h before starting the measurements in order to ensure a steady state.
2. Carrying out the polarization curves and the potentiostatic EIS at OCV in $H_2/H_2$ mode (proton pump) for the anode impedance from $f = 100$ kHz to $f = 0.1$ Hz with 10 points per decade and an amplitude of 4 mV.
3. Switching back to $H_2/N_2$ mode, waiting for 10 min and carrying out potentiostatic EIS for $R_\Omega$ and $R_p$. Then, recording CVs to determine the hydrogen permeation properties, the roughness factor *rf* (or electrochemical surface area, ECSA) and the double layer capacity. This step was explained in detail in our previous publication.[7] Hereafter, going back to the first step with the next humidity and temperature condition.

In a second measurement campaign in $H_2/H_2$ mode we also implemented recovery steps to avoid CO-poisoning of the catalyst layers (see below for further details).

The main test run in fuel cell mode was done with 7 humidity conditions, from $rH = 30\%$ to $rH = 100\%$, 4 temperatures ($T = 50$ °C to $T = 80$ °C), 4 concentrations on the cathode side ($x^{dry}_{O_2} = 1$, $x_{O_2} = 0.5$, $x_{O_2} = 0.25$, $x_{O_2} = 0.16$), and 16 current densities ($j = 2\ A\ cm^{-2}$ to $j = 4\ mA\ cm^{-2}$), leading to 1792 operating points. For our EIS measurements we chose 10 currents out of the 16 ($j = 2\ A\ cm^{-2}$ to $j = 20\ mA\ cm^{-2}$), leading to 1120 spectra. The constant dry flow rates were 1300 sccm on the anode side and 2000 sccm on the cathode side and the system pressure was $p_{total} = 1.5\ bar_a$, leading to pressure drops $\Delta p < 100$ mbar for all the conditions. To vary $p_{O_2}$ we mixed $O_2$ with $N_2$ ahead of the humidification bubbler, and we also conducted heliox measurements in a separate experiment for $rH = 30\%$ and $rH = 80\%$. The run was carried out in the order of increasing dew points and from high currents to low currents. Whenever adjusting the temperature or the dew point, the cell was stabilized in $H_2$/air at 0.7 V for 2 h. The currents at which we performed EIS were stabilized for 25 min prior to the measurement to ensure high measurement quality, and the other currents were held for 5 min. The impedance measurements were carried out in hybrid mode with 11 mV AC amplitude from $f = 100$ kHz to $f = 0.1$ Hz and with 10 points per decade. We also calculated the distribution of relaxation times to deconvolute the physicochemical processes, given by

$$Z_{DRT}(f) = R_\Omega + \int_{-\infty}^{+\infty} \frac{\gamma \ln(\tau)}{1 + i2\pi f\tau} \mathrm{d}(\ln \tau) \qquad [2]$$

For this, we used the tool by Wang et al.[42] which we have adapted to allow an automated evaluation of multiple spectra at the same time (See Figs. S2a to S2d).

Finally, we performed steady-state limiting current (SLC) measurements according to the method proposed by Baker et al.[38] and transient limiting current (TLC) measurements as proposed by Göbel et al..[40] We chose to carry out the SLC measurements for 4 pressure levels ($p_{total} = 1.5,\ 2,\ 3,\ 4\ bar_a$), 3 humidity levels ($rH = 30,\ 80,\ 100\%$), 4 temperature levels ($T = 50,\ 60,\ 70,\ 80$ °C) and 4 concentrations ($x_{O_2} = 0.02,\ 0.05,\ 0.1,\ 0.15$). For stabilizing the operating conditions, the same procedures and times as mentioned above were used. Before going to the limiting current, the cell was held at 0.7 V for 8 min at given pressure, humidity, temperature and concentration. Then, the voltage was set to 0.3 V for 5 min, 0.2 V for 5 min and 0.15 V for 5 min and the limiting current was determined from these three operating points. The TLC measurements were carried out for $x_{O_2} = 0.16$ and $x_{O_2} = 0.25$ at $p_{total} = 1.5\ bar_a$ by conditioning the cell current for 10 min and going to the limiting current for 10 s in the potentiostatic mode. Since in limiting current operation the conditions were not differential anymore, we considered a log-averaged $O_2$ concentration to calculate the transport resistance $R_{MT}$.

An overview on how we ensured good measurement quality (state-of-health checks and Kramers-Kronig test) is given in the supplementary material of this work (see Fig. S3). Furthermore, we show the methodology used to extract the kinetic parameters for the anode and cathode kinetics based on a flowchart in Fig. 11 in the appendix.

## Results and Discussion

***Ionomer properties.***—In order to carry out loss analyses, the Ohmic resistance $R_\Omega$ containing the electronic losses and the protonic losses of the membrane, as well as the effective protonic resistance of the CCL $R^{eff}_p$, have to be known for each condition. These two resistances cause a voltage loss that is proportional to the cell current density as $\Delta U = j \cdot (R_\Omega + R^{eff}_p)$. Further, it is essential to correct the cell current for the hydrogen crossover current $j_{H_2,crossover}$ for accurate Tafel analyses of the ORR at small current densities. We characterized these ionomer properties extensively in our previous publication and provide a brief summary of the parameterized models in the supplementary material (see Fig. S4).[7] Also, the EIS spectra of an *rH*-variation under load for two currents and their DRTs are shown exemplarily in Fig. S5 to illustrate the importance of the ionomer humidification on the performance .

***Anode contribution.***—Since the Pt-loading in our anode is eight times lower than the loading in the cathode, we did not expect the anode overpotential to be completely negligible during normal fuel cell operation, even though the Pt-area specific exchange current density of the HOR is several orders of magnitude higher than the one of the ORR. Thus, we carried out measurements in the $H_2/H_2$ configuration to investigate the anode contribution to the overall cell performance. Due to the fast diffusion of $H_2$ from the channel to the ACL and the thinness ($\approx 2\ \mu$m) of the electrode in our system, we neglect mass transport and assume that the anode impedance is limited by proton transport within the ACL and by the electrochemical oxidation of hydrogen according to

$$H_2 \rightleftharpoons 2H^+ + 2e^- \quad [3]$$

In previous works, the $H_2$ kinetics was generally assumed to be describable by a sequence of two out of the three following reaction pathways:

$$\text{Tafel:} \quad H_2 \rightleftharpoons 2H_{ad} \quad [4]$$

$$\text{Heyrovsky:} \quad H_2 \rightleftharpoons H_{ad} + e^- + H^+ \quad [5]$$

$$\text{Volmer:} \quad H_{ad} \rightleftharpoons H^+ + e^- \quad [6]$$

There have been many studies focusing on nailing down the exact reaction mechanism and trying to find out whether the hydrogen adsorption on the metal or the electron transfer step is dominant (see references in Table I). The latest research of Stühmeier et al. showed that a Tafel-Volmer mechanism is most likely to occur within the anode of PEM fuel cells at small overpotentials.[14] However, the HOR is often described by a single Butler-Volmer (BV) law in the modeling literature for the sake of simplicity. Moreover, since the kinetics are typically operating in the linear regime over a large current density range, the Butler-Volmer expression can even be linearized. Thus, the overall voltage loss contribution from the anode reaction (in fact including the effect of proton transport limitations in the ACL) is written as

$$\eta_{anode} = \frac{RT}{F j^0_{a,eff}(\alpha_c + \alpha_a)} \cdot j \quad [7]$$

where both the current density $j$ and the effective exchange current density $j^0_{a,eff}$ are referenced to the geometrical surface area. The sum of anodic and cathodic transfer coefficients ($\alpha_c + \alpha_a$) cannot be determined from the linear regime and is set to unity in this case.[14] Table I summarizes various parameterizations of the HOR/HER from the literature that were referenced to the platinum surface area for the sake of comparableness ($rf = 30\ m^2_{Pt}/m^2_{geo}$ for our measurements). However, due to the likely inhomogeneous through-plane-distribution of the reaction rate, this approach to reference the exchange current density presumably introduces errors and makes the comparison between values from different sources difficult. The above expression of the overpotential leads to the impedance of the charge transfer process

$$\frac{\partial \eta_{anode}}{\partial j} = R_{anode} = \frac{RT}{F j^0_{a,eff}} \rightarrow j^0_{a,eff} = \frac{1}{R_{anode}} \cdot \frac{RT}{F} \quad [8]$$

which does not depend on the current density. This means that the exchange current density can be parameterized by EIS and that measurements at OCV are sufficient. Further, it means that the Tafel slope (symmetry factor) is not accessible from these measurements and that we get no information regarding the rate limiting step.

Figure 3a shows the EIS at OCV and Fig. 3b the corresponding DRT of a relative humidity variation at 80 °C with pure $H_2$ on both sides. As can be seen from these typical $H_2/H_2$ spectra, two main processes are identified, which confirms previous literature findings.[9,15–17] Apparently, both processes exhibit a strong humidity dependency. For the high-frequency loop, this dependency is believed to come from the proton transport resistance of the catalyst layer,[18] or from a water dependency in the hydrogen kinetics itself.[53] However, EIS and DRT results from a humidity variation with a low $p_{H_2,anode}$ (see Figs. S6a to S6b) show that the high frequency loop in fact contains two processes with separate time constants and that only the one occurring at the highest frequencies seems to be humidity-dependent. This hints at combined *rH*-dependent proton transport and *rH*-independent electrode kinetics, thus confirming the former hypothesis. In Fig. 3c we fitted the HF loop ($R_{P1A} = R_{HF}$) to the low-frequency real part of the transmission line model

$$Z = \sqrt{R_p R_{ct}} \coth\left(\frac{R_p}{R_{ct}}\right) \quad [9]$$

and assumed that the cathode impedance (counter electrode) is negligible (due to its eight times higher ECSA), which was previously discussed in the literature for comparable counter electrodes.[52] Here, $R_{ct}$ represents the kinetics charge transfer resistance and $R_p$ the proton resistance of the catalyst layer. The Fig. shows the resistance over *rH* at 80 °C for three different $H_2$ concentrations on the anode side ($x_{H_2,A} = 0.75$, $x_{H_2,A} = 0.5$ and $x_{H_2,A} = 0.25$, obtained by diluting with $N_2$). We further assumed that the proton resistance is a fraction of the cathode proton resistance we characterized in blocking cathode configuration[7] and found $R_{p,anode} = 0.18 \cdot R_{p,cathode}$, reflecting approximately the ratio of anode to cathode thickness ($2/13 \approx 0.15$). The HF loop is therefore well explained by a combination of proton transport and charge transfer limitations as given by Eq. 9. It is worth noting that we generally found $R_{ct}$ to be in the same order of magnitude or smaller ($1\ m\Omega\ cm^2 < R_{ct} < 30\ m\Omega\ cm^2$) than $R_p$ ($7\ m\Omega\ cm^2 < R_p < 60\ m\Omega\ cm^2$). In this limit $R_p > R_{ct}$, Eq. 9 simplifies to $Z = \sqrt{R_p \cdot R_{ct}}$, such that the true exchange current density $j^0_{a,ct} = RT/(F \cdot R_{ct})$ is related to the apparent exchange current density by $j^0_{a,ct} = j^0_{a,eff} \cdot \sqrt{R_p/R_{ct}}$.

Even though Neyerlin et al.[52] explained that with pure hydrogen the gas-phase related transport resistances are expected to be very small in the proton pump measurements with state-of-the-art diffusion media (high diffusion coefficient $D_{H_2} \approx 0.5\ cm^2/s$),[52] Heinzmann et al. recently showed that low-frequency EIS loop depends on the partial pressure and assigned it to $H_2$ mass transport from the channel to the reaction sites.[18] We also see this $p_{H_2}$-dependency of the LF loop (see below); however, the influence of *rH* is just as strong in our case. In the literature, this dependency on *rH* was attributed to ionomer dry out effects caused by the electro-osmotic drag.[54,55] Based on these analyses, we believe that the interplay of $R_p$ and $R_{ct}$ in the transmission line causes the combined *rH* and $p_{H_2}$ influence on the low-frequency loop. The other hypotheses of the low frequency process being linked to $H_2$ adsorption or desorption processes,[15,16] or to the HER,[10] could not be validated yet. Further parameter variations in the $H_2/H_2$ configuration can be seen in the supplementary material (Figs. S6 and S7).

When trying to characterize the temperature dependency of the anode kinetics, we were initially puzzled by a far too high apparent activation energy of $E_{act} > 70\ kJ\ mol^{-1}$ in our first two $H_2/H_2$ measurement campaigns. We already observed this high *T*-dependency during the $H_2/N_2$ characterization in our previous publication[7]. After identifying an undesired and highly *T*-dependent anodic contribution via EIS, we chose to account for it through an additional R-CPE element in order to achieve a clean parameterization of the ionomer resistance $R_p$. We also found that this spurious process was correlated to long stabilization times ($> 2$ h) prior to the measurements and that it was in fact due to CO poisoning of the catalyst layer. This poisoning effect is absent in the normal fuel cell configuration since $O_2$ crossover from the cathode to the anode helps

**Table I. HOR and/or HER data from the literature. Data obtained from measurements in acidic and in alkaline media as well as in full PEM fuel cells. In PEMFCs, the $j_0$ values are given for $p_{H_2} \approx 1$ bar and the information on the catalyst are only given for the working electrode if not mentioned otherwise (A stands for anode and C stands for cathode).**

| Catalyst | Electrolyte | $T$ (°C) | $j^0_{a,eff}$ (mA $cm^{-2}_{Pt}$) | $E_{act}$ (kJ $mol^{-1}$) | Tafel slope (mV/dec) | Year / References |
|---|---|---|---|---|---|---|
| 5wt% Pt/C | 96% $H_3PO_4$ | 160 | 144 | 17 | 43[a)] | 1975 / [43] |
| Mono- & Polycrystalline Pt | $HCLO_4$ | 25 | 1.7–3 | | 30 | 1987 / [44] |
| Polycrystalline Pt | 0.01 N $HCLO_4$ | 25 | 2.48 | | 118[b)] | 1989 / [45] |
| | 0.01 N—0.1 N $H_2SO_4$ | | 1.75–1.16 | | | |
| | 0.1 N $H_3BO_3$ | | $\ll 0.01$ | | | |
| | 0.08 N NaOH | | 0.55 | | | |
| Monocrystalline Pt | 0.5 M $H_2SO_4$ | 25 | ≈1–1.5 | | 32-35 | 1992 / [46] |
| Monocrystalline Pt | 0.05 M $H_2SO_4$ | 60 | 0.83–1.35[c)] | 9.5–18[c)] | 28–112[c)] | 1997 / [47] |
| 1.7 mg $cm^{-2}$ symmetrical | PEMFC (N112) | 50 | 7[d)] | | | 1999 / [15] |
| 20wt% Pt/C, 0.5 mg $cm^{-2}$ | 1 M $H_2SO_4$ | 25 | 1 | | | 2001 / [48] |
| 47wt% Pt/C, 0.05–0.4 mg $cm^{-2}$ | PEMFC (900EW) | 60 | ≈27[e)] | 9.5 | 33 | 2004 / [49] |
| 10wt% $Pt_{nano}$/C | 0.10 M $H_2SO_4$ | 25 | ≈ 20 | | 30 | 2004 / [50] |
| 0.7 mg $cm^{-2}$ symmetrical | PEMFC (N117) | 40–70 | 2.6 mA/$mg_{Pt}$[f)] | 50–55 | | 2005 / [17] |
| Polycrystalline Pt | 0.15 M $HCLO_4$ | 25 | 1.08 | | | 2006 / [8] |
| 50wt% Pt/C, 0.35/0.5 mg $cm^{-2}$ (A/C) | PEMFC (1100EW) | 80 | 7–36 A/$mg_{Pt}$[g)] | | | 2007 / [51] |
| 5wt% Pt/C, 0.003 mg $cm^{-2}$ | PEMFC | 80 | 235–600 | | 70–140 | 2007 / [52] |
| Symmetrical, Pt/C | HT-PEM (PBI/$H_3PO_4$) | 80–140 | 550–1450 | | | 2009 / [10] |
| 46wt% Pt/C, 0.007 mg $cm^{-2}$ | 0.1 M KOH | 21 | 0.57 | 30 | 120 | 2010 / [11] |
| 4.7wt% Pt/C, 0.002 mg $cm^{-2}$ | PEMFC | 40-80 | 120–260 | 16 | 124–149 | 2014 / [12] |
| 0.2/0.4 mg $cm^{-2}$ (A/C) | PEMFC | 80 | ≈ 19 A/$mg_{Pt}$[h)] | | | 2018 / [18] |
| 4.8wt% Pt/C, 1.2–1.6 $\mu$g $cm^{-2}$ | PEMFC | 30–90 | 88–580 | 25 | 135–144 | 2021 /[14] |
| 0.05/0.4 mg $cm^{-2}$ (A/C) | PEMFC | 40–80 | 170–408[i)] | 17.8[i)] | | This work |

a) Determined with $2.3RT/(2F)$ for 160 °C. b) Determined with $2.3RT/(0.5F)$ for 25 °C. c) Dependent on the different Pt facets. d) Determined by $j_0 = RT/(zFR_a)$, with $R_a$ being the resistance of the HF loop. e) Data taken from[47] for Pt(110) ($j_0 = 1.35$ mA $cm^{-2}_{Pt}$) and adjusted to match the observed polarization curves. f) Calculated based on the HF loop at 60 °C. Since *rf* is not given, data is mass specific. g) Based on the polarization curves slopes for 60% *rH* and 100% *rH* (12 mΩcm$^2$ and 2.5 mΩcm$^2$). Values obtained by considering the ratio of loadings of the electrodes. Since *rf* is not given, data is mass specific. h) Estimated for $\approx (0.4/(0.4 + 0.2)) \cdot 12$ mΩcm$^2$ at OCV in $H_2/H_2$, $T = 80$ °C, $p_{H_2} = 0.67$ bar and $rH = 70\%$. i) Values obtained for our final test run containing micropolarization curves, EIS and recovery steps to keep the catalyst layers clean. Calculated for $rf$=30 $m^2_{Pt}/m^2_{geo}$ obtained by CV measurements.

keeping the anode catalyst clean. It also perfectly explains the observed high $T$-dependency.[56] We refer to the supplementary material for a more detailed discussion.

To get a clean dataset we reproduced $H_2/H_2$ EIS and micropolarization measurements and introduced recovery steps after each operating condition to keep the catalyst layers clean. To do so, we carried out CV measurements from −0.9 V to 0.9 V to oxidize the CO layer in both the anode and cathode electrode by diluting $H_2$ in $N_2$ and stopping the flow before starting the measurements. Such a CV measurement is shown in Fig. 4a, where the CO peaks are highlighted by the gray areas and disappear completely after the second cycle. We chose $rH = 100\%$ in this test run to keep the ionomer resistances as low as possible and therefore make the evaluation of the kinetics as precise as possible. In Fig. 4b we show the micropolarization curves of a hydrogen partial pressure variation at $rH = 100\%$ and $T = 40$ °C and Fig. 4c displays corresponding EIS at OCV. The polarization curves show a perfectly linear behavior in the range that we used for the parameter fitting; however, the HOR direction (negative voltage and current in this case) shows non-linearities at higher overpotentials for the low $H_2$ concentrations. In this special case, this behavior is not linked to the anodic overpotential-dependent limiting current observed in the literature (most probably potential-independent rate limiting Tafel step),[12,14] but rather to mass transport contributions because of the dropping stoichiometry ($\lambda < 4$). In the Nyquist plot of the EIS measurements at OCV, we can only observe one loop at high partial pressures. With decreasing partial pressures, several capacitive processes and a low-frequency inductive feature appear. According to detailed analyses of these EIS features (see Fig. S8), the high-frequency loop has an activation energy of around 20 kJ $mol^{-1}$ which is much higher than for the low-frequency capacitive loop (≈2 kJ $mol^{-1}$) and for the low-frequency inductive loop (≈4 kJ $mol^{-1}$). Moreover, the size of the inductive loop is inversely proportional to $p_{H_2}$ (exponent ≈−1.0) and therefore stronger pressure-dependent than the capacitive loops (exponent ≈−0.8).

However, for fitting our simple kinetics model we chose to evaluate the polarization curves. The according procedure for extracting the parameters is shown in the appendix in Fig. 11. Figure 5a shows an Arrhenius plot of the HOR/HER exchange current density for three different concentrations and the corresponding Ohmic resistance used for the performance corrections. The resulting activation energies are virtually independent of $p_{H_2}$ and lie in the range 15 kJ $mol^{-1}$ to 18 kJ $mol^{-1}$, which is close to the value from Durst et al..[12] Fig. 5b shows the partial pressure dependency of the exchange current density (apparent reaction order with respect to $p_{H_2} \approx 0.4$) at $T = 40$ °C. This is in line with the results of Stühmeier et al..[14] At lower partial pressures the apparent exchange current density deviates from the expected behavior and gets too small. This effect partially comes from the presence of the other effects that are also visible in the EIS response as mentioned above. If we analyze only the high-frequency loops from the EIS (triangles in Fig. 5b), the exchange current densities are closer to the regression curve but still too low. This effect may come from a change in the influence of the ionomer contribution on the effective anode resistance when the charge transfer resistance rises due to lower $p_{H_2}$, such that the approximation $R_p > R_{ct}$ of Eq. 9 is not justified anymore. Another possible explanation is a change in the mechanisms of the kinetics at very low partial pressures. However, the current parameterization of the hydrogen kinetics is already sufficiently accurate in the range of operating conditions that are meaningful for typical PEM operation. Hence, we chose to exclude all the data points recorded at $p_{H_2} < 0.1$ bar in our final fitting and obtained the expression

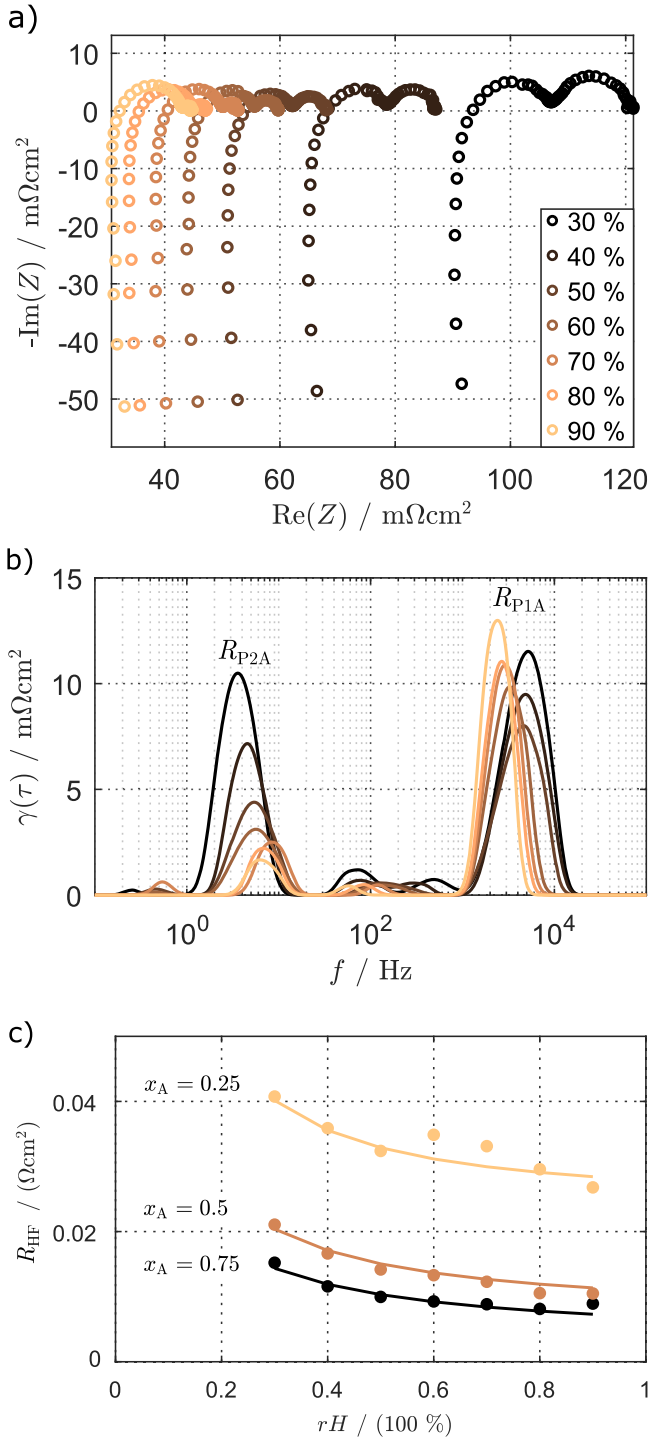


**Figure 3.** a) EIS for a variation of $rH$ in $H_2/H_2$ mode at OCV ($U_{cell} = 0$ V) and $T = 80$ °C with pure $H_2$ on both sides ($x_{H_2}^{dry} = 1$). b) DRT corresponding to a). c) Transmission line model based fits of the HF loop resistance $R_{P1A}$ in $H_2/H_2$ mode at OCV and $T = 80$ °C with pure $H_2$ in the cathode for three $H_2$ concentrations in the anode $x_A$.

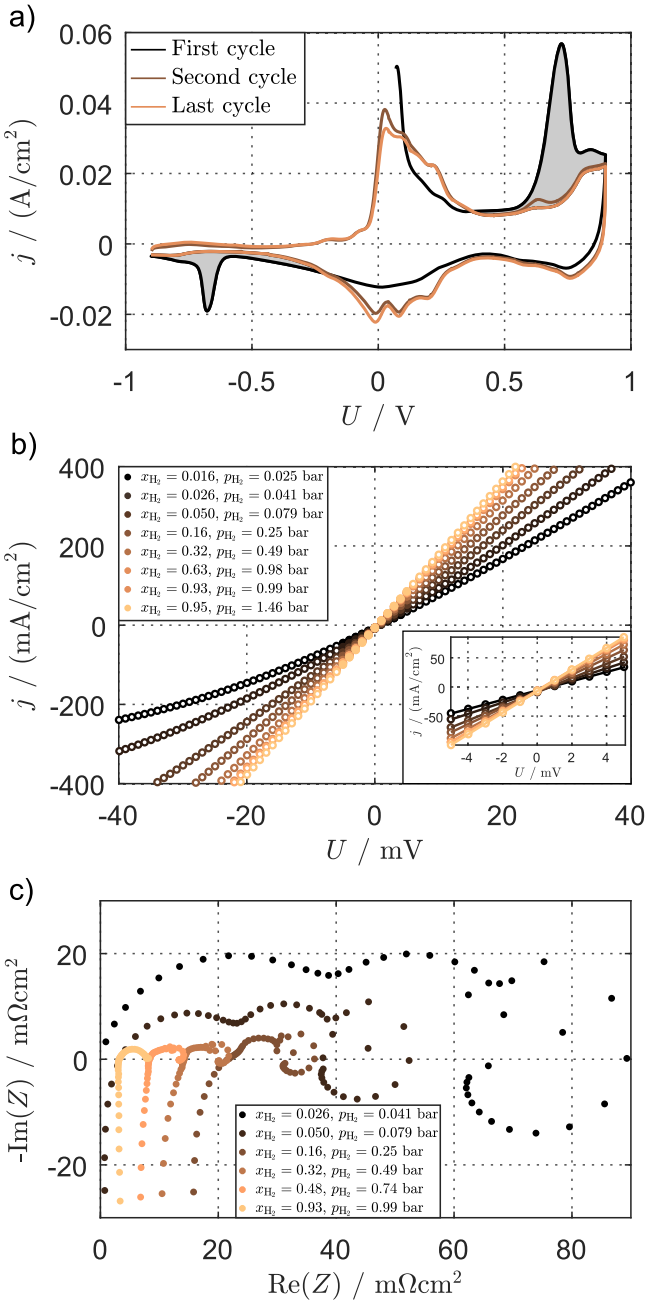


**Figure 4.** a) CO recovery step: combined CV of the anode and cathode catalyst layer during proton pump operation with 2.7% $H_2$ in the dry {$H_2$, $N_2$} mixture at $p_{total} = 1.5$ $bar_a$, $rH = 100\%$ and $T = 40$ °C. The scan was carried out with 100 mV $s^{-1}$ from −0.9 V to 0.9 V after stopping the gas streams. In this case, the conditions were held over 10 h before the measurement to exaggerate the poisoning effect and demonstrate the efficacy of the method. After the 2nd cycle, the CO peaks have completely disappeared. b) Micropolarization curves for a $p_{H_2}$ variation at $T = 40$ °C where the inset represents a zoom on the voltage zone used for parameterization. c) EIS at OCV for a $p_{H_2}$ variation at the same conditions as in d). The curves are shifted along the $x$-axis for the sake of visibility.

$$j^0_{a,eff} = (1.57{\cdot}10^2\ \mathrm{A/cm^2_{Pt}}){\cdot}\left(\frac{p_{H_2}}{p_{ref}}\right)^{0.36} \exp\left(-\frac{17.8\ \mathrm{kJ\ mol^{-1}}}{RT}\right) \quad [10]$$

which was normalized by the roughness factor 30 $m^2_{Pt}$ $m^{-2}_{geo}$ (see above). The correlation plot in Fig. 5c demonstrates the model and the measured values match quite well apart from the points that were excluded from the fitting. Further, the resulting fit parameters are close to the values from the literature for proton pumping experiments (see Table I).[12,14,52] Nevertheless, we emphasize that if we consider the true exchange current density $j^0_{a,ct} = (j^0_{a,eff})^2{\cdot}R_p{\cdot}F/(RT)$ instead of the apparent exchange current density $j^0_{a,eff}$, the activation energy becomes 23.4 kJ $mol^{-1}$ and the reaction order with respect to hydrogen doubles

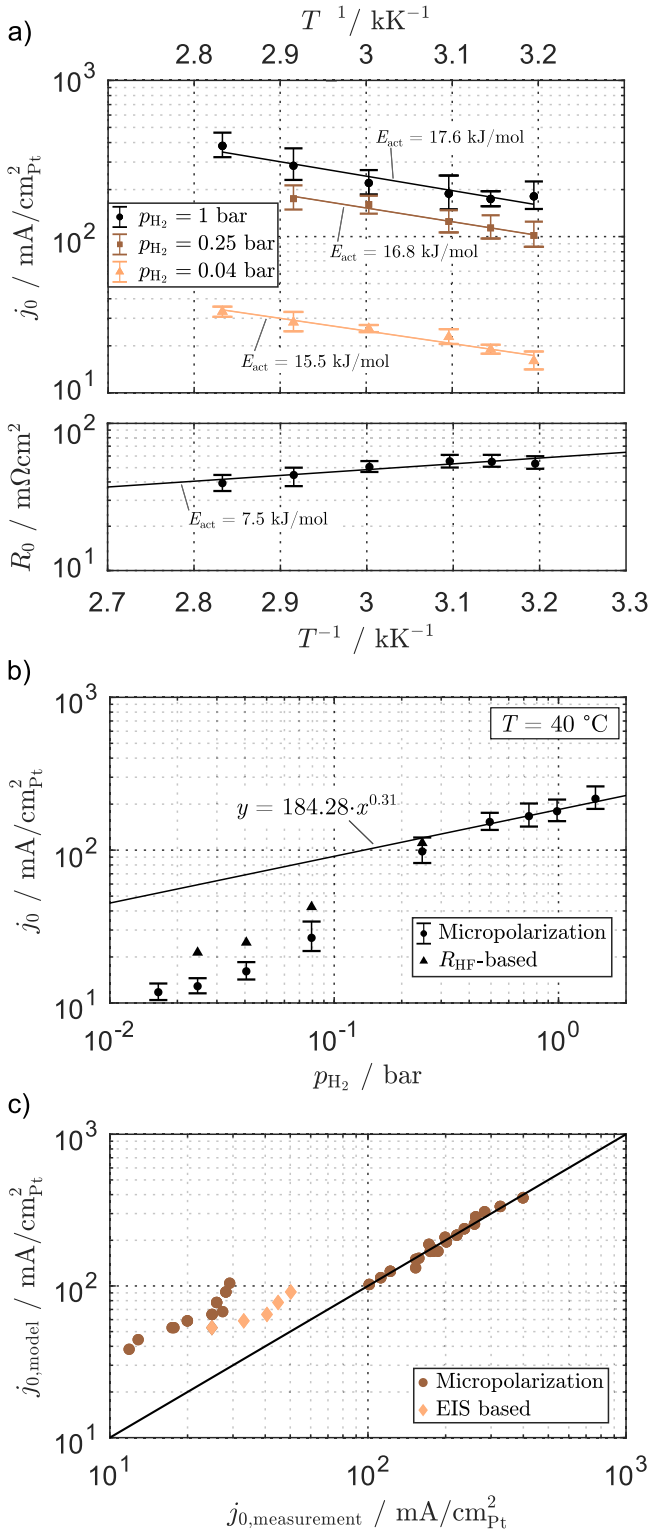


**Figure 5.** a) Arrhenius plot of the HOR/HER specific current density for three $H_2$ concentrations and corresponding high-frequency resistance below. b) Double-logarithmic plot of the specific current density over $p_{H_2}$ at $T = 40$ °C. The error bars in a) and b) have been determined over at least two measurements. c) Correlation plot of the specific exchange current density obtained from the fitted model versus the values calculated based on our measurements. In all the plots, $j_0 = j^0_{a,eff}$.

from 0.36 to 0.72. Further, the true exchange current density is two to three times higher ($j^0_{a,ct} \approx 1$ A cm$^{-2}_{Pt}$) than the apparent exchange current density ($j^0_{a,eff} \approx 0.4$ A cm$^{-2}_{Pt}$) at the same conditions.

With this evaluation we obtain a ready-to-use model for the anode kinetics that can directly be implemented into simulation models or used for loss contribution analyses. Furthermore, we emphasize the importance of our CO recovery procedure for getting accurate data and that caution is required even when working at high cell temperatures since surface poisoning effects can easily be overlooked.

***Cathode kinetics.***—The ORR is the major loss process under the most relevant operating conditions. Thus, well-parameterized models are needed for the ORR to accurately predict the performance in fuel cell operation. As mentioned in the introduction, this is still subject to research as there is no consensus regarding its mechanistic description. However, simple Tafel kinetics is typically employed since the overpotential $\eta_{ORR}$ is high and can be expressed as a logarithmic function of the current density according to

$$\eta_{ORR} = \frac{RT}{\alpha_c F} \cdot \ln \frac{j}{j^0_{c,eff}} \quad [11]$$

where the cathodic transfer coefficient $\alpha_c$ is the product of the symmetry factor $\beta$ and the number of transferred electrons $z$, and $j^0_{c,eff}$ is the effective exchange current density. This leads to the impedance expression of the charge transfer process

$$\frac{\partial \eta_{ORR}}{\partial j} = R_{ct} = \frac{RT}{\alpha_c F j} = \frac{b}{j} \quad [12]$$

that does not depend on the exchange current density $j^0_{c,eff}$ and thus not on $p_{O_2}$. This expression directly links the intrinsic Tafel slope $b$ (slope of the curves $U_{jR-free}$ versus $\ln(j + j_{H_2,crossover})$) to the size of the charge transfer loop in the Nyquist spectra. In contrast to the anode kinetics (see Eqs. 7 and 8), EIS cannot be used to determine the exchange current density, yet would enable direct characterization of $b$. However, this is complicated by the impact of slow Pt oxidation kinetics on the apparent Tafel slope in steady-state measurements.[57] These oxidation mechanisms lead to low-frequency inductive features in the EIS spectra and discrepancies are therefore observed between an EIS-based evaluation of $b$ through the high-frequency charge transfer resistance $R_{ct}$ by $b = j \cdot R_{ct}$ and a steady-state-based evaluation of $b$ trough the slope of the polarization curve in the Tafel plot. The first approach yields Tafel slopes $b \geqslant 100$ mV/dec (see Fig. S5), and the second approach yields slopes $b \approx 70$ mV/dec (see below). We will analyze this effect in a forthcoming paper. In the present work, we aim for a simple representation of the ORR kinetics and understanding of its limits by parameterizing a Tafel law like shown in Eq. 11 using exclusively polarization data at low currents.

We evaluated the kinetics overpotential $\eta_{ORR}$ by subtracting the $jR$-free voltage from the equilibrium voltage $U_0$ according to

$$\begin{aligned} \eta_{ORR} &= U_0 - U_{measurement} + j \cdot (R_p^{eff} + R_\Omega) \\ &= U_0 - U_{jR-free} \end{aligned} \quad [13]$$

where the $jR$-correction was made based on the evaluation of EIS spectra under load as described in our previous publication.[7] In the literature, the ORR parameters are most often obtained from measurements gathered under fully saturated conditions[19] and a full factorial parameterization containing data at varying $rH$ does not exist to our knowledge; however, some authors discussed the influence of $rH$ on the ORR performance. Xu et al. found out that their CCL performs badly at elevated temperature and dry conditions even after correcting the data for the effective protonic resistance.[58,59] In contrast to these findings, Neyerlin et al. and Liu et al. saw a way smaller influence of $rH$ on the $jR$-free performance.[60,61] Even though the humidity influence on the ORR initially appeared to be small in our dataset (see Fig. S9a), we

investigated different modeling approaches. Firstly, we used an approach were the water activity was set to unity as it is usually the case in literature studies which we call here the 'water-independent' approach. There, the equilibrium voltage $U_0$ can be calculated by the Nernst equation according to

$$U_0 = 1.23\ \text{V} - (0.9\cdot10^{-3}\ \text{VK}^{-1})(T - 298\ \text{K}) + \frac{RT}{2F}\ln\left[\left(\frac{p_{H_2}}{p_{ref}}\right)\left(\frac{p_{O_2}}{p_{ref}}\right)^{\frac{1}{2}}\right] \quad [14]$$

The exchange current density contains the dependencies on temperature and on oxygen partial pressure through the activation energy $E_{act}$ and the reaction order $\gamma$, respectively, and was expressed as

$$j^0_{c,eff} = rf\cdot j^0_{c,ref}\cdot\left(\frac{p_{O_2}}{p_{ref}}\right)^{\gamma}\exp\left[\frac{-E_{act}}{RT}\left(1 - \frac{T}{T_{ref}}\right)\right] \quad [15]$$

with *rf* the roughness factor of the cathode electrode in $m^2_{Pt}\ m^{-2}_{geo}$ and $j^0_{c,ref}$ the reference exchange current density in $A\ cm^{-2}_{Pt}$. In our second approach that we call in the following 'water-dependent' we accounted for the actual partial pressure of water in the gas phase $p_{H_2O}$ in the Nernst equation instead of setting the activity to unity and thus calculated the cell equilibrium voltage by

$$\tilde{U}_0 = 1.23\ \text{V} - (0.9\cdot10^{-3}\ \text{VK}^{-1})(T - 298\ \text{K}) + \frac{RT}{2F}\ln\left[\left(\frac{p_{H_2O}}{p_{ref}}\right)^{-1}\left(\frac{p_{H_2}}{p_{ref}}\right)\left(\frac{p_{O_2}}{p_{ref}}\right)^{\frac{1}{2}}\right] \quad [16]$$

We further added a possible water dependency in the exchange current density through a power law for $p_{H_2O}$ therein with the supplementary parameter $n$. This change yields

$$\tilde{j}^0_{c,eff} = rf\cdot j^0_{c,ref}\cdot\left(\frac{p_{H_2O}}{p_{ref}}\right)^{n}\cdot\left(\frac{p_{O_2}}{p_{ref}}\right)^{\gamma} \times\exp\left[\frac{-E_{act}}{RT}\left(1 - \frac{T}{T_{ref}}\right)\right] \quad [17]$$

Therefore, the basic model for saturated conditions contains the four fitting parameters $\alpha_c$, $E_{act}$, $\gamma$, and $j^0_{c,ref}$, and the modified $p_{H_2O}$-dependent model adds a fifth parameter, $n$. It can easily be shown algebraically however that for $n = 0.5$ both models are in fact identical. Thus, a noticeable water dependency is only observed if $n \neq 0.5$.

We depict the method to get the kinetic parameters schematically in Fig. 11 of the appendix. If not mentioned otherwise, the reference conditions for all fitted models were $T_{ref} = 80\ °C$ and $p_{ref} = 1$ bar. We took $j = j_{measured} + j_{H_2,crossover}$ for the global fitting and excluded $j > 0.1\ \ A\ cm^{-2}_{geo}$ in most cases. To verify the meaningfulness of the latter condition and see the influence of one-at-a-time parameter variations, we performed local fits at given humidity, temperature or current density (see Table S1 and Table S2 of the supplementary material) prior to the global fit over all the conditions simultaneously. These local fits confirmed that the parameters are constant and the Tafel slope was captured properly for $j \leqslant 0.1\ \ A\ cm^{-2}$. The model for the $H_2$ permeation coefficient $\Psi_{H_2}$ and the corresponding measurements are summarized in Fig. S4c over $T$ and $rH$ and the resulting crossover current taken for the current correction is shown in Fig. S4d for our standard condition $p_{total} = 1.5\ \ bar_a$. Since the membranes of our samples showed very high electrical resistances ( $\gg 600\ \Omega\ cm^2$) we neglected electrical membrane shorts.

Optimized parameters from the global fit simultaneously over all the operating conditions are shown in Table II. It can be seen that the activation energy is around $70\ kJ\ mol^{-1}$, the reference exchange current density is around $2\cdot10^{-8}\ A\ cm^{-2}_{Pt}$, the reaction order is around 0.5 and the exponent of the power law for the water partial pressure dependency is between 0.4 and 0.5. Moreover, the fit results from cases in which $\alpha_c$ was not fixed to 1 (not shown in the table) yielded results that were very close to those of the fitting procedures in which $\alpha_c$ was fixed to 1, matching our expectations of Tafel slopes around 70 mV/dec (see above). Figures 6a and 6b show the good agreement between the fitted local exchange current densities (symbols, $\alpha_c = 1$) and the global model (black lines) for an *rH* variation with the $p_{H_2O}$-dependent model at $T = 50\ °C$ and $T = 80\ °C$ (Fig. 6a) and with the $p_{H_2O}$-independent model (Fig. 6b) at the same conditions. The $rH = 90\%$ conditions are outliers and thus were excluded from the fitting (probably partial flooding of the electrode). In Fig. 6c and Fig. 6d we depict a $p_{O_2}$ variation for four different temperature and humidity combinations for the $p_{H_2O}$-dependent model and the $p_{H_2O}$-independent model, respectively (see Fig. S9b for a similar plot in the heliox case). The slopes in the double-logarithmic plots of this Fig. represent the reaction order $\gamma$ (for the $p_{O_2}$ variation) and the exponent of the $p_{H_2O}$ influence $n$ (*rH* variation). Both models seem to fit the data well. This is not surprising, as $n \approx 0.5$ means that both models are essentially equivalent and there is effectively no influence of *rH* on the ORR. Thus, the exchange current density can be parameterized as

$$\tilde{j}^0_{c,eff} = rf\cdot(2.13\cdot10^{-8}\ A\ /cm^2_{Pt})\left(\frac{p_{H_2O}}{p_{ref}}\right)^{0.51}\left(\frac{p_{O_2}}{p_{ref}}\right)^{0.49} \times\exp\left[\frac{-68.7\ kJ\ mol^{-1}}{RT}\left(1 - \frac{T}{T_{ref}}\right)\right] \quad [18]$$

if the Nernst equation contains the effective water partial pressure, or as

$$j^0_{c,eff} = rf\cdot(2.15\cdot10^{-8}\ A\ /cm^2_{Pt})\left(\frac{p_{O_2}}{p_{ref}}\right)^{0.51} \times\exp\left[\frac{-71.3\ kJ\ mol^{-1}}{RT}\left(1 - \frac{T}{T_{ref}}\right)\right] \quad [19]$$

if the water activity is set to unity in the Nernst equation.

**Table II. Exchange current density parameters extracted from globally fitting all the polarization points $U_{jR-free}$ for $j \leqslant 0.1\ A\ cm^{-2}$. The conditions where no *n* is given were fitted with the $p_{O_2}$-independent model (water activity set to unity in $U_0$ and $j^0_{c,eff}$). The symmetry factor was fixed at $\alpha_c = 1$.**

| $\alpha_c$ (—) | $j^0_{c,ref}\cdot10^8$ ($A/cm^2_{Pt}$) | $\gamma$ (—) | $n$ (—) | $E_{act}$ ($kJ\ mol^{-1}$) |
|---|---|---|---|---|
| | $p_{H_2O}$-dependent model without the $rH = 90\%$ conditions | | | |
| 1.0 | 2.13 | 0.49 | 0.51 | 68.74 |
| | $p_{H_2O}$-dependent model with all conditions | | | |
| 1.0 | 1.82 | 0.50 | 0.41 | 73.41 |
| | $p_{H_2O}$-independent model with all the *rH* conditions | | | |
| 1.0 | 2.05 | 0.50 | —- | 69.52 |
| | $p_{H_2O}$-independent model only with $rH = 80\%$ conditions | | | |
| 1.0 | 2.15 | 0.51 | —- | 71.27 |
| | $p_{H_2O}$-independent model only with $rH = 90\%$ conditions | | | |
| 1.0 | 1.81 | 0.54 | —- | 70.88 |

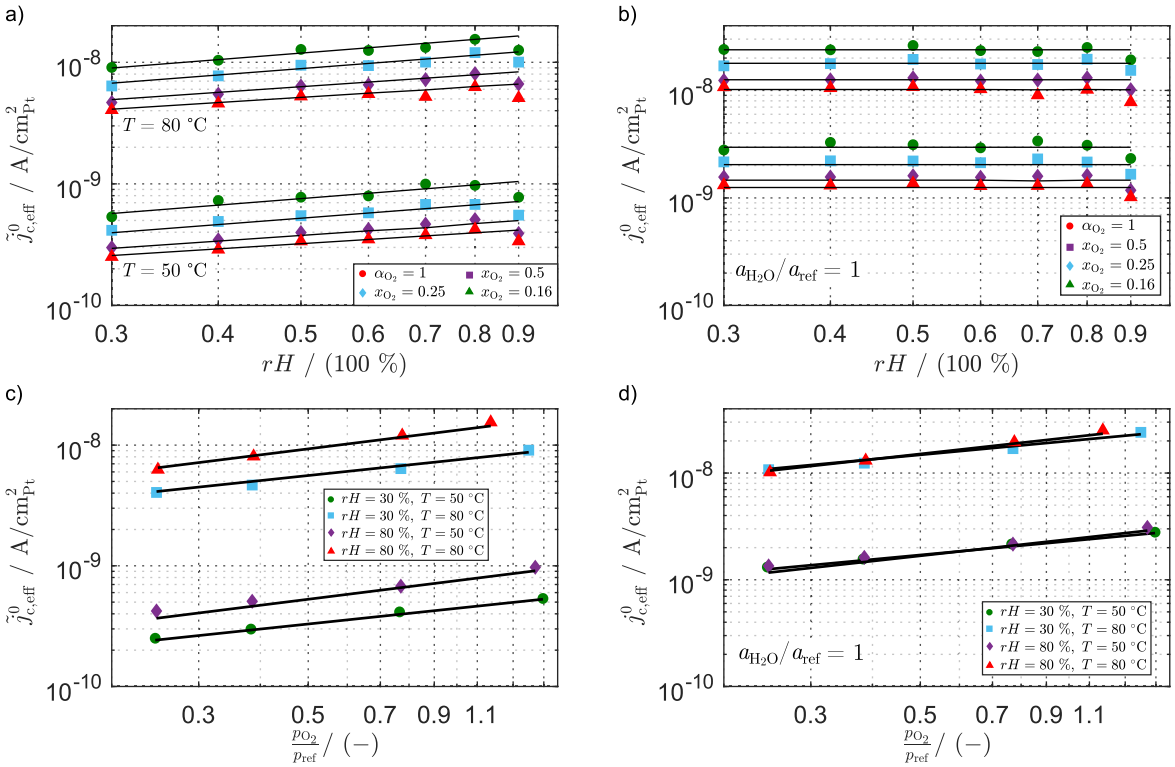


**Figure 6.** Local exchange current densities (symbols) and global model (lines) for the {$O_2$,$N_2$} measurements. a) $p_{H_2O}$-dependent model for $T = 50$ °C and $T = 80$ °C over the relative humidity *rH*. Both the Nernst voltage $\tilde{U}_0$ and $\tilde{j}^0_{c,eff}$ depend on the water partial pressure. b) Same as in a) for the $p_{H_2O}$-independent model where liquid water is assumed in the Nernst voltage and in the expression of the model of $j^0_{c,eff}$ (activity is set to unity) instead of using $p_{H_2O}$ in the gas phase. c) Same as in a) for a $p_{O_2}$ variation at four different temperature and humidity levels. d) Same as in c) for the $p_{H_2O}$-independent model.

Figure 7a depicts the measured exchange current density versus the modeled exchange current density for the $p_{H_2O}$-dependent model and Fig. 7b for the $p_{H_2O}$-independent model. The measured $U_{jR-free}$ cell voltage versus the modeled cell voltage is also shown for both model variants in Figs. 7c and 7d. Even though both models yield very good agreement with the experimental data, the water-dependent model seems to slightly outperform the water-independent model, which is not surprising considering the additional degree of freedom in the fitting procedure. Figure S9c to S9f additionally depict the good match between measured $U_{jR-free}$ polarization curves and the according model curves at four different *rH* and *T* combinations (exemplarily for the water-dependent model). Furthermore, we checked our specific values against the data published by Neyerlin et al.[19] that still represent a reliable reference to date for Pt/C catalysts. This comparison is given in Table III: first, we compared the exchange current density parameters referenced to 80 °C and 1 bar; second, we compared the *jR*-free cell voltage referenced to 80 °C 1 bar and 0.9 V. The equation for the latter was given as in Eq. 20:[19]

$$U_{jR-free} = 0.9\ \text{V} - \frac{RT}{\alpha_c F} \ln\left[\frac{j + j_{crossover}}{rf \cdot j^{0.9V}_{0,ref} \cdot \left(\frac{p_{H_2}}{p_{ref}}\right)^{\alpha_c/2} \left(\frac{p_{O_2}}{p_{ref}}\right)^{m} \exp\left[\frac{-E^{0.9V}_{act}}{RT}\left(1 - \frac{T}{T_{ref}}\right)\right]}\right] \quad [20]$$

Table III shows that there is a good agreement between the reference from the literature and our measurements. Hence, we have an accurate ready-to-use model for the ORR mechanism in our full cell described by a simple Tafel law with an intrinsic slope determined by $\alpha_c = 1$. This model can reasonably be applied over a wide range of current densities ($U_{jR-free} > 0.8$ V) and, according to the literature, more complex models with ORR intermediates only gain importance with low-loaded cathodes or at lower potentials.[27] Subramanian et al. parameterized oxide-coverage-dependent ORR kinetics to model their *jR*-corrected performance curves measured with a cathode loading of 0.06 mg $cm^{-2}_{geo}$.[27] This model contains a change in the apparent Tafel slope at around 0.75 V to 0.8 V and they ruled out mass transport effects in their measurement based on limiting current measurements. In our data, we also see deviations from the ORR model below 0.8 V. These effects could also result from more complex ORR kinetics, from inaccurate *jR* corrections at high current densities (decreasing fitting quality with decreasing CCL utilization), or from mass transport contributions. A more detailed discussion regarding these observations is given below.

***Mass transport contributions.***—Investigating the contribution to the cell resistance of $O_2$ mass transport from the gas channels to the catalytic surface of the Pt particles is essential for modeling purposes since it usually contributes to the overpotential at operating conditions that are relevant from a system point of view (medium to high current densities). Furthermore, the importance of this contribution grows as the roughness factor decreases,[62] which is a main target to pursue for cost-reductions. In this work, we want to clarify whether $O_2$ transport contributions are relevant in the ORR parameterization to ensure that the parameters are free of unwanted effects. For this purpose, both the steady-state limiting current (SLC) technique and the transient limiting current (TLC) technique are used and discussed. The principle of the first method lies in measuring the limiting current density with strongly diluted oxygen to avoid high currents and therefore much water production (dry transport resistance), whereas the principle of the second method lies in recording a limiting current density for an arbitrarily conditioned cell state by going to a low cell voltage only for a few seconds ($< 10$ s) in order not to significantly change the cell state. In our case, the TLC was measured along polarization curves for different operating

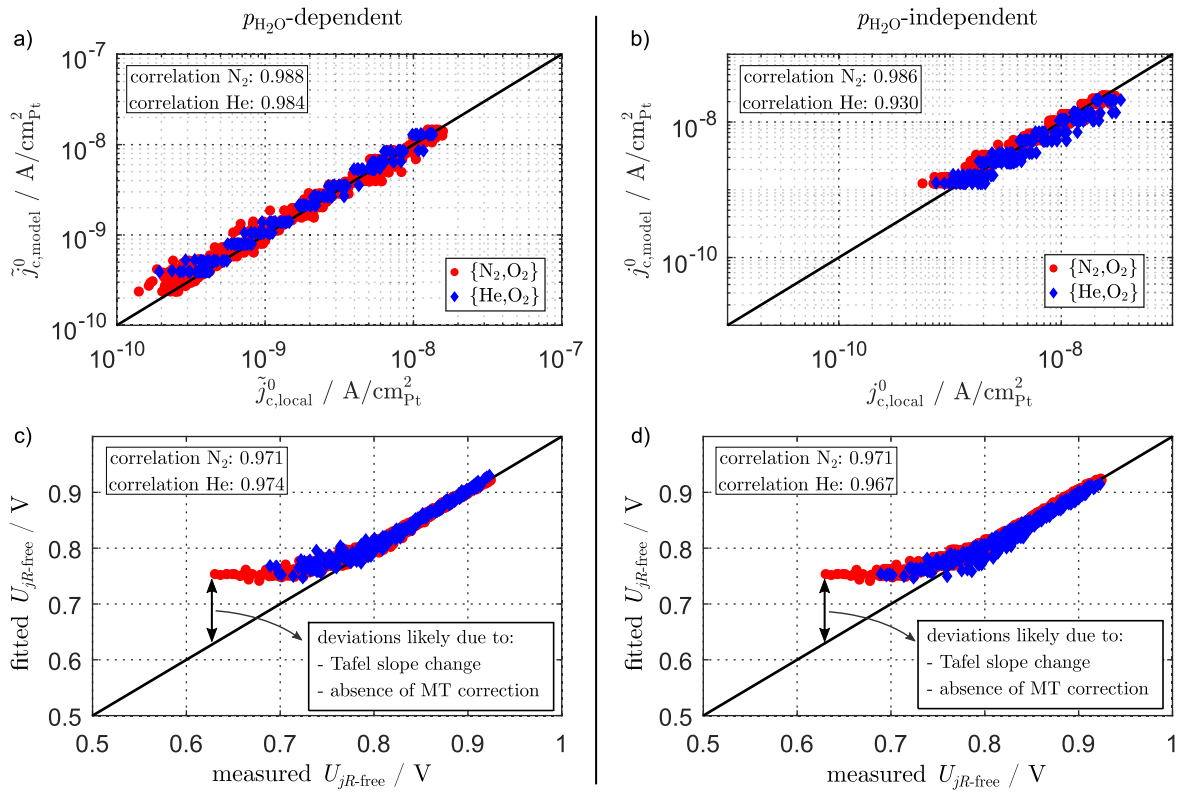


**Figure 7.** a) Correlation plot of the ORR exchange current density $\tilde{j}^0_{c,eff}$ (local measurement vs. model) with the $p_{H_2O}$-dependent model. b) Same as in a) with the $p_{H_2O}$-independent model ($j^0_{c,eff}$). In a) and b), the local exchange current density was calculated for all the currents $j < 1$ A cm$^{-2}$. c) Correlation plot of $U_{measurement} = U_{jR-free}$ vs. $U_{model} = U_0 - \eta_{ORR,model}$ for all the conditions (and current densities) with the $p_{H_2O}$-dependent model. d) Same as in c) with the $p_{H_2O}$-independent model. The plots a) and b) contain each 783 {$O_2$,$N_2$} data points and 168 {$O_2$,He} data points and the plots c) and d) contain each 1117 {$O_2$,$N_2$} data points and 240 {$O_2$,He} data points.

**Table III. Comparison of our reference data ($rH = 80\%$) with the data of Neyerlin et al..[19] The parameters were acquired by fitting Eq. 15 and Eq. 20 to our data.**

| Parameter | Neyerlin[19] | This work | |
|---|---|---|---|
| | | {$O_2$,$N_2$} | {$O_2$,He} |
| Exchange current density parameters | | | |
| $j^0_{c,ref} \cdot 10^8$ (A/cm$^2_{Pt}$) | 2.47 | 2.15 | 2.45 |
| $\gamma$ (—) | 0.54 | 0.51 | 0.62 |
| $E_{act}$ (kJ mol$^{-1}$) | 67 | 71.27 | 68.62 |
| $U_{jR-free}$ parameters | | | |
| $j^{0.9V}_{0,ref} \cdot 10^4$ (A/cm$^2_{Pt}$) | 2.47 | 2.11 | 2.49 |
| $m$ (—) | 0.79 | 0.75 | 0.87 |
| $E^{0.9V}_{act}$ (kJ mol$^{-1}$) | 10 | 10.85 | 10.89 |

parameters to investigate the impact of current density on the transport resistance.

We measured steady-state limiting currents for strongly diluted $O_2$ in $N_2$ gas streams and different temperature and humidity levels according to the method described by Baker et al..[38] During this procedure, the cell was operated up to the $O_2$ mass transport limitation (vertical part of the polarization curve at high currents) by jumping to cell voltages below 0.3 V in the potentiostatic mode. Low oxygen concentrations are used to avoid high limiting currents and therefore much liquid water production that would alter the measured transport resistance in the gas phase. From this limiting current density the oxygen transport resistance (in s/m) from the channel to the electrode can be calculated by

$$R_{O_2,MT} = \frac{p_{O_2}^{channel} \cdot 4 \cdot F}{R \cdot T \cdot j_{lim}} \quad [21]$$

Since the conditions were not perfectly differential during the limiting current measurements, we chose to use a log-mean $O_2$ partial pressure in the gas channel which was calculated based on the inlet and the outlet mole fraction. The outlet mole fraction was estimated by

$$x_{O_2}^{outlet} = \frac{\dot{n}_{O_2}^{inlet} - j_{lim}/(4 \cdot F)}{\dot{n}_{O_2}^{inlet} + \dot{n}_{N_2} + \dot{n}_{H_2O}^{inlet} + j_{lim}/(4 \cdot F)} \quad [22]$$

with $\dot{n}$ being the molar fluxes and under the assumption that the product water is completely in the gas phase on the cathode side, $\dot{n}_{H_2O}^{outlet} = \dot{n}_{H_2O}^{inlet} + j_{lim}/(2 \cdot F)$. Based on such an $O_2$ transport resistance from limiting current experiments, it is possible to estimate the voltage drop during a polarization curve by considering both the effect on the Nernst voltage and the drop of the exchange current density of the ORR:

$$\Delta U_{O_2,MT}(j) = \frac{RT}{F}\left(\frac{1}{4} + \frac{\gamma_{ORR}}{\alpha_{ORR}}\right) \ln\left(\frac{p_{O_2}^{in} - \frac{RT}{4F} \cdot R_{O_2} \cdot j}{p_{O_2}^{in}}\right) \quad [23]$$

Here, $\gamma_{ORR} = 0.5$ is the ORR reaction order and $\alpha_{ORR} = 1$ the ORR transfer coefficient. In Fig. 8a we depict the measured transport resistance $R_{O_2,MT}$ over the limiting current density $j_{lim} \propto x_{O_2}$ for 80% and 100% $rH$ and four temperatures ($T = 50$ °C to $T = 80$ °C). As expected, the resistance grows with decreasing temperature, which can be attributed to the decreasing diffusion coefficients. Also, the

80%-*rH* resistances seem to be located in an intermediate range between dry conditions and fully saturated conditions as they converge to very low values at low limiting currents and to similar values as for 100% *rH* at high limiting currents. We also observed such a transition behavior between a dry and a wet plateau in our transient limiting current measurements (see Fig. 8c). Such behavior is known in the literature for some GDLs.[39,40,63,64] As the resistances are below 1 s cm$^{-1}$ even at fully satured gas and low temperature conditions, the loss contributions will be very small at typical operating conditions.

In Fig. 8b we show the voltage drop occasioned by $O_2$ transport over the current density for four different temperature and humidity combinations, which reflects the higher transport resistances of the fully saturated conditions. Owing to the fact that the loss contribution initially increases linearly, it is very small in the low current density range ($j < 0.5$ A cm$^{-2}$) no matter the temperature and partial pressure. In the range that is interesting for our ORR investigations, the voltage drop does not exceed 3 mV and is therefore not significant for the ORR parameterization. Subramanian et al. used such SLC measurements as an argument to exclude the possibility of $O_2$-transport-related effects in the change of the apparent Tafel slope they observed experimentally (mainly with their low-loaded cathode).[27] However, according to us there are two uncertainties coming with such considerations. First, the resistance from the SLC experiment does not correspond to the resistance along the polarization curve since it is a function of saturation and temperature of the porous media and therefore depends on current density. This is indicated in Fig. 8c, where the transient limiting current measurements show the significant influence of the pre-polarization current on the mass transport resistance. Secondly, we might underestimate the resistance and mainly characterize the GDL resistance because the oxygen concentration may drop toward zero at the CL/GDL boundary during limiting current operation such that the catalytic reaction concentrates near that interface. Thus, the measured resistance may not contain the CCL resistance that is effective during a normal polarization curve in the non-transport-limited region. Moreover, even though $R_{O_2,MT}$ in the SLC case (Fig. 8a) seems to converge to similar values as the wet plateaus in the TLC case (Fig. 8c) at high limiting currents (and thus high $O_2$ concentrations), the TLC resistances are higher than the SLC resistances at low currents, indicating a different water management in the cell. This effect was also observed by Göbel et al.[40] but is not yet well enough understood. Therefore, the polarization curve corrections based on limiting current techniques have to be interpreted with caution. However, mass transport corrections of the performance based on both the SLC and the TLC technique are discussed below. For the SLC method we parameterized a model of the transport resistance $R_{O_2,MT}$ by fitting it to the values measured for the highest $O_2$ concentration (highest limiting current and thus highest resistance) $x_{O_2} = 0.15$, over all the humidity, temperature, and total pressure levels (see above for the values). For this model we got

$$R_{O_2,SLC} = (8.74\cdot10^{-1}\ \text{s/cm})(rH)^{0.07}\left(\frac{p_{total}}{p_{ref}}\right)^{0.87} \times \exp\left(\frac{10.7\ \text{kJ mol}^{-1}}{RT}\right) \quad [24]$$

with $p_{ref} = 1$ bar$_a$. The good match between this model and the measured data is shown in Fig. 9.

***Loss contributions analysis.***—Finally, we show typical *jR*-corrected polarization curves for the $N_2$ and the He cases in Fig. 10a ($T = 50$ °C, $rH = 80\%$) and Fig. 10b ($T = 80$ °C, $rH = 80\%$) for all our $O_2$-concentration levels in the Tafel representation. These polarization curves show that the kinetics part at low currents can be accurately described by a Tafel slope of around 70 mV/dec, which meets our expectations. Moreover, the use of helium instead of nitrogen does not seem to influence the kinetics part ($j \leqslant 0.2$ A cm$^{-2}$ at $T = 50$ °C and $j \leqslant 0.5$ A cm$^{-2}$ at $T = 80$ °C) and starts to have an influence at current densities above 0.3 A cm$^{-2}$. While the heliox curves clearly show less voltage loss at high current

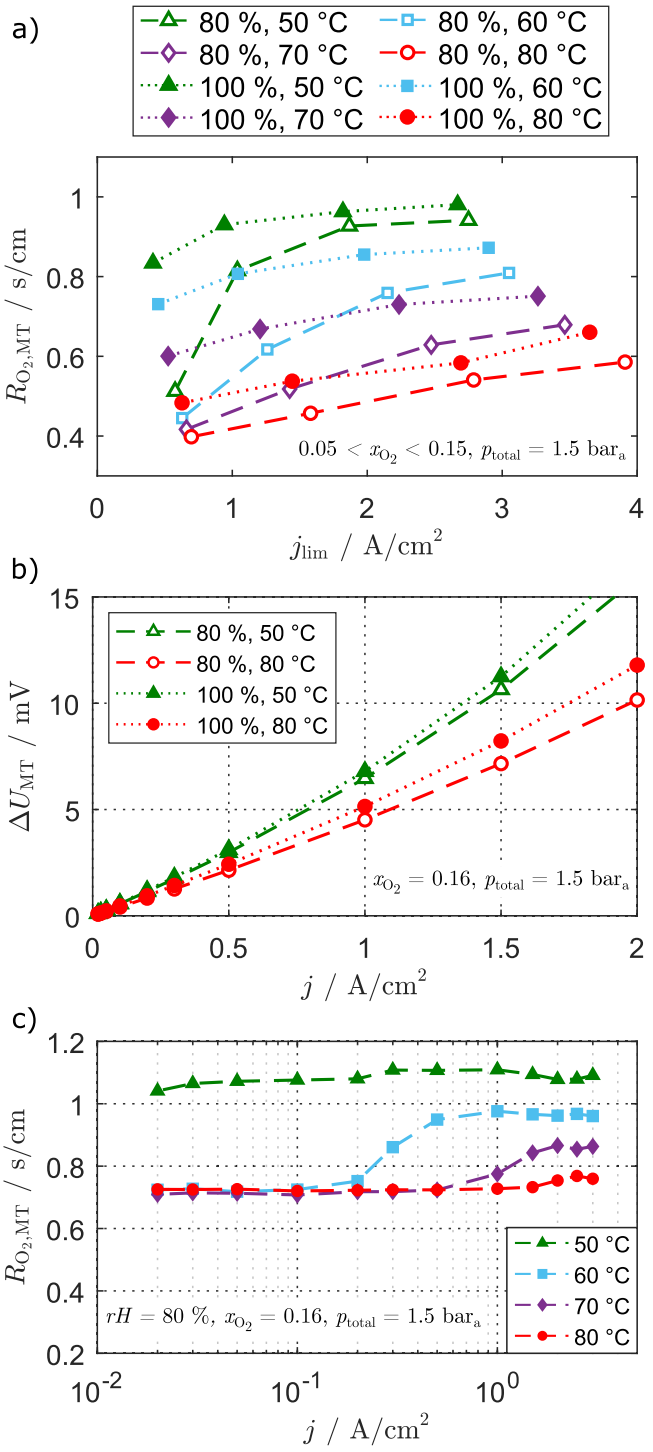


**Figure 8.** a) Oxygen mass transport resistance $R_{O_2,MT}$ from steady-state limiting current measurements in fuel cell configuration depending on the limiting current density for different temperature and humidity conditions at $p_{total} = 1.5$ bar$_a$. The variation of the limiting current was achieved by varying the oxygen mole fraction in the gas stream. b) Voltage loss contribution from $O_2$ transport over the current density for four different humidity and temperature combinations, estimated for $x_{O_2} = 0.16$. c) $R_{O_2,MT}$ from transient limiting current measurements over the conditioning current density at $rH = 80\%$, $p_{total} = 1.5$ bar$_a$ and $x_{O_2} = 0.16$ for four temperatures.

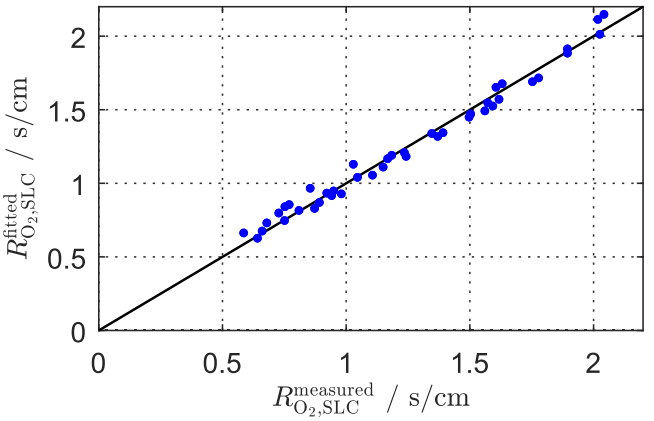


**Figure 9.** Correlation plot of $R^{\text{measured}}_{O_2,SLC}$ versus $R^{\text{fitted}}_{O_2,SLC}$ for $x_{O_2} = 0.15$ and all the *rH*, *T* and $p_{\text{total}}$ levels.

densities, deviations from ideal Tafel behavior still remain in this region. Plausible explanations would be either pressure-independent transport effects (platinum-near effects that are unaffected by the use of heliox) or intrinsic changes of the ORR Tafel slope. Interestingly, the deviations are more important at cold conditions, where the diffusion coefficients are the lowest and two-phase issues (liquid water) the most pronounced. Also, the $x^{\text{dry}}_{O_2} = 1$ curves are parallel to the $x_{O_2} = 0.5$ curves with nitrogen but the distance between the $x^{\text{dry}}_{O_2} = 1$ curves and the $x_{O_2} = 0.5$ curves with helium decreases over the current density. One explanation for this effect could be a different water management with the helium mixture since the diffusion coefficient of water in helium is roughly ten times higher than the one of water in nitrogen ($3.1 \cdot 10^{-4}$ m$^2$s$^{-1}$ for He against $3.9 \cdot 10^{-5}$ m$^2$s$^{-1}$ for $N_2$ at 300 K) and the thermal conductivity of helium is roughly six times higher than the one of nitrogen(157 mWm$^{-1}$K$^{-1}$ for He against 26 mWm$^{-1}$K$^{-1}$ for $N_2$ at 300 K and 2 bar).[65] Fig. 10c exhibits a typical polarization curve for $x_{O_2} = 0.16$ with its according *jR* correction, anode correction based on our parameterization of the HOR, and mass transport correction based either on the SLC method (curve i) or on the TLC method (curve ii). One can see that even for this humid condition ($rH = 80\%$), the major loss mechanism apart from the ORR still comes from the protonic losses in the membrane and cathode catalyst layer over a wide range of current densities. Figure 10c further confirms that voltage losses from anode kinetics and mass transport are negligible at the lowest current densities used for the parameterization of the ORR kinetics. Across our full factorial DOE, the voltage losses from these effects at $j = 1$ A cm$^{-2}$ do not exceed 5 mV ($\approx 4.6$ mV at $T = 50$ °C and $\approx 2.5$ mV at $T = 80$ °C, anode kinetics) and 7 mV (mass transport, based on SLC measurements), respectively. At higher current densities however, these losses gain in importance and thus meaningful characterization is needed in order not to draw wrong conclusions. Even though the Ohmic contributions and the HOR kinetics are properly accounted for, the mass transport loss correction brings uncertainties in the analysis: while the SLC-corrected curve predicts a deviation from the Tafel line beyond 0.5 A cm$^{-2}$, the TLC-corrected curve lies on the Tafel line over the whole current density range. Further measurement techniques such as EIS could be brought into play to strengthen the investigation of mass transport contributions. Nevertheless, the model for $R_{O_2}$ parameterized by SLC measurements (see Eq. 24) can be employed to delimit the performance range in which the ORR obeys a simple Tafel law for sure, which corresponds to steady-state cathodic half-cell potentials above 0.8 V in our case as shown in Fig. 10d.

## Conclusions

In this work, we extensively studied the hydrogen and oxygen kinetics as well as oxygen mass transport contributions in a

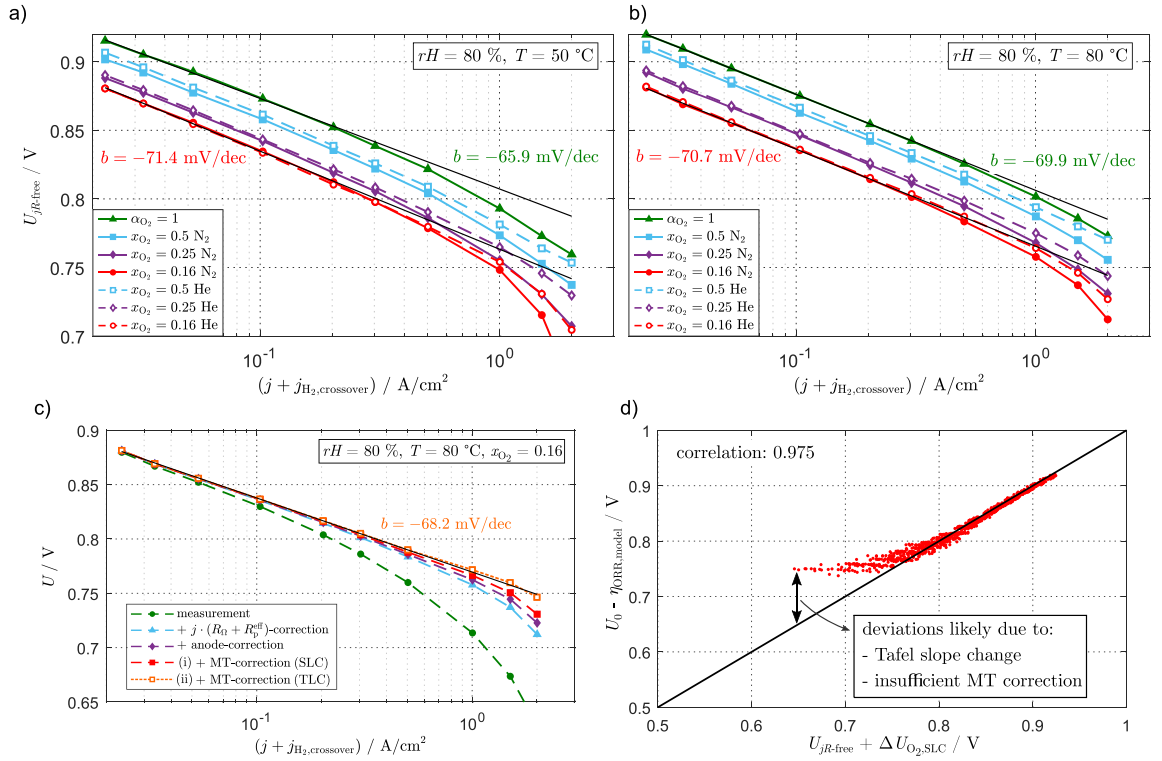


**Figure 10.** Polarization curves in the Tafel representation. a) *jR*-free curves for our four $O_2$ concentrations in the {$O_2$, $N_2$}-mixture and comparison with the same concentrations in the {$O_2$, He}-mixture at $rH = 80\%$ and $T = 50$ °C. b) Same as in a) but at $rH = 80\%$ and $T = 80$ °C. c) Polarization curve for $x_{O_2} = 0.16$ at $rH = 80\%$ and $T = 80$ °C with its different levels of loss-corrections. d) Correlation plot of $U_{\text{measurement}} + j \cdot (R_p^{\text{eff}} + R_\Omega) + \Delta U_{O_2,SLC}$ vs. $U_{\text{model}} = U_0 - \eta_{ORR,\text{model}}$ for all the conditions with the $p_{H_2O}$-independent model. The mass transport correction was calculated by Eqs. 23 and 24.

differential PEM fuel cell with a state-of-the-art MEA based on an unprecedentedly large dataset. Systematic parameter variations ($rH$, $T$, $p_{O_2}$, $p_{H_2}$, $j$) were conducted and polarization data and EIS were recorded.

EIS in the Proton pumping mode ($H_2/H_2$) allowed us to better understand the performance signatures. With the help of DRT and by fitting a classical TLM to the data, we assigned the high-frequency loop to a combination of $H_2$ kinetics (strongly $p_{H_2}$ dependent) and proton transport in the catalyst layer (strongly $rH$ dependent). We pointed out that the definition of the effective exchange current density therefore depends on the conductivity of the ionomer in the anodic catalyst layer. Even though we could not finally assign the low-frequency loop to a specific process, we showed that it is strongly influenced by both $p_{H_2}$ and $rH$. We further found that CO surface poisoning can, in the absence of oxygen, severely impede the HOR kinetics and distort its characterization when overlooked, even at high temperatures. We introduced a fast and simple recovery procedure to oxidize parasitic CO almost simultaneously in both electrodes. This allowed us to get an accurate parameterization of the HOR (linearized Butler-Volmer consideration) in our full cell that can be used for loss contribution analyses and physical cell models.

Subsequently, a full factorial parameterization of the ORR mainly based on steady-state data obtained in the $H_2/O_2$ mode with $\{O_2, N_2\}$ or $\{O_2, He\}$ mixtures on the cathode side provided a simple and accurate parameterization of the ORR kinetics based on a simple Tafel law with an exchange current density depending on $p_{O_2}$ and temperature. Detailed analysis of its humidity dependency and comparison of $p_{H_2O}$-dependent and $p_{H_2O}$-independent models showed that it is justified to simply assume a constant water activity in modeling approaches even under dry conditions.

Furthermore, we quantified the oxygen mass transport contributions to the overall cell voltage through steady-state and transient limiting current measurements. In combination with the previously developed models of the HOR and ORR, this permitted a quantitative analysis of the different loss mechanisms occurring in the cell and confirmed that the anode and mass transport contributions do not interfere with an ORR parameterization based on current densities $j \leqslant 0.1$ A cm$^{-2}$. For the whole range of conditions covered by our full-factorial test procedure, the simple Tafel law accurately captures the (steady-state) ORR kinetics down to cathodic half-cell potentials of 0.8 V, without the need to account for intrinsic changes of the ORR Tafel slope. In the region of lower half-cell potentials and thus typically high current densities, the analysis becomes limited by uncertainties in the accounting of mass transport effects. This is because readily available techniques are not able to probe mass transport alone without at the same time affecting the internal state of the porous structures (water and heat management), as demonstrated by our comparison of steady-state and transient limiting current data, and our observations on heliox measurements.

However, our large set of EIS data revealed systematic trends on the dynamical response of the ORR reaction that are not covered by the simple Tafel law, even at low current densities. Further, observed discrepancies between Tafel slopes from polarization-based data and EIS-based evaluations hint at more complex electrode kinetics and shall be addressed in our next publication.

## Acknowledgments

The authors thank SGL® Carbon for providing the gas diffusion layer samples and Gore® for helpful discussions.

## Appendix

The flowchart in Fig. 11 shows the methods we use to fit our kinetics parameters depending on the electrode being investigated and whether an analytical expression of the overpotential $\eta$ is known. Since in this work we employed simple Tafel kinetics for the ORR, which yields such an analytical relation for $\eta_{ORR}$, we only needed the paths that are inside the frame. However, our general

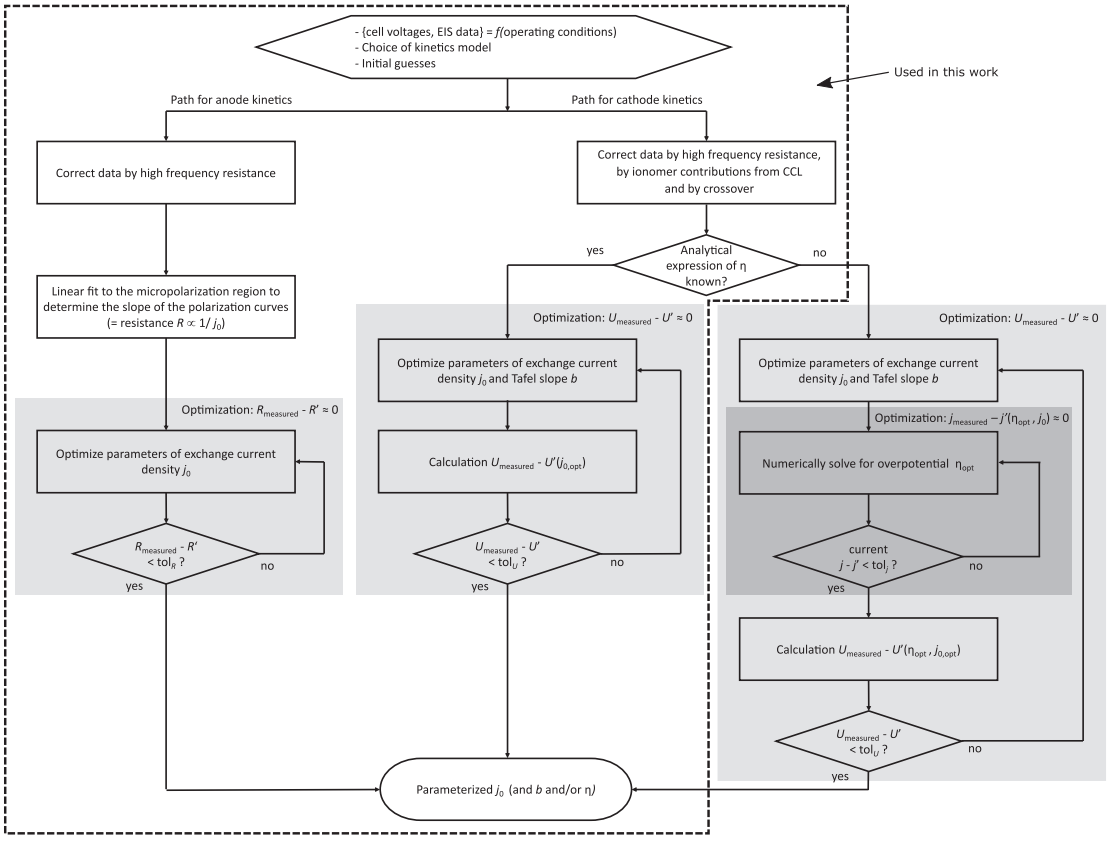


**Figure 11.** Flowchart representing the routines used in this work to extract kinetics parameters.

approach enables also to test other formulations of the ORR, which is not in the scope of this publication.

## ORCID

Christophe Gerling https://orcid.org/0000-0002-7918-6973

## References


1. Y. Wang, D. F. Ruiz Diaz, K. S. Chen, Z. Wang, and X. C. Adroher, "Materials, technological status, and fundamentals of PEM fuel cells - A review." *Mater. Today*, **32**, 178 (2020).
2. T. E. Springer, "Polymer Electrolyte Fuel Cell Model." *J. Electrochem. Soc.*, **138**, 2334 (1991).
3. M. Eikerling and A. Kornyshev, "Modelling the performance of the cathode catalyst layer of polymer electrolyte fuel cells." *Journal of Electroanalytical Chemistry*, **453**, 89 (1998).
4. L. Carrette, K. A. Friedrich, and U. Stimming, "Fuel Cells - Fundamentals and Applications." *Fuel Cells*, **1**, 5 (2001).
5. R. Vetter and J. O. Schumacher, "Experimental parameter uncertainty in proton exchange membrane fuel cell modeling. Part I: Scatter in material parameterization." *Journal of Power Sources*, **438**, 227018 (2019).
6. E. J. F. Dickinson and G. Smith, "Modelling the Proton-Conductive Membrane in Practical Polymer Electrolyte Membrane Fuel Cell (PEMFC) Simulation: A Review." *Membranes*, **10**, 310 (2020).
7. C. Gerling, M. Hanauer, U. Berner, and K. A. Friedrich, "Full factorial in situ characterization of ionomer properties in differential PEM fuel cells." *J. Electrochem. Soc.*, **168**, 0845 (2021).
8. A. F. Innocente and A. C. D. Ângelo, "Electrocatalysis of oxidation of hydrogen on platinum ordered intermetallic phases: Kinetic and mechanistic studies." *Journal of Power Sources*, **162**, 151 (2006).
9. D. Malevich, E. Halliop, B. Peppley, J. Pharoah, and K. Karan, "Effect of Relative Humidity on Electrochemical Active Area and Impedance Response of PEM Fuel Cell.." *ECS Trans.*, **16**, 1763 (2019).
10. A. Huth, B. Schaar, and T. Oekermann, "A proton pump concept for the investigation of proton transport and anode kinetics in proton exchange membrane fuel cells." *Electrochimica Acta*, **54**, 2774 (2009).
11. W. Sheng, H. A. Gasteiger, and Y. Shao-Horn, "Hydrogen Oxidation and Evolution Reaction Kinetics on Platinum: Acid vs Alkaline Electrolytes." *J. Electrochem. Soc.*, **157**, B1529 (2010).
12. J. Durst, C. Simon, F. Hasché, and H. A. Gasteiger, "Hydrogen oxidation and evolution reaction kinetics on carbon supported Pt, Ir, Rh, and Pd electrocatalysts in acidic media." *J. Electrochem. Soc.*, **162**, F190 (2014).
13. V. Briega-Martos, A. Ferre-Vilaplana, E. Herrero, and J. M. Feliu, "Why the activity of the hydrogen oxidation reaction on platinum decreases as pH increases." *Electrochimica Acta*, **354**, 136620 (2020).
14. B. M. Stühmeier, M. R. Pietsch, J. N. Schwämmlein, and H. A. Gasteiger, "Pressure and Temperature Dependence of the Hydrogen Oxidation and Evolution Reaction Kinetics on Pt Electrocatalysts via PEMFC-based Hydrogen-Pump Measurements." *J. Electrochem. Soc.*, **168**, 064516 (2021).
15. M. Ciureanu and H. Wang, "Electrochemical Impedance Study of Electrode-Membrane Assemblies in PEM Fuel Cells: I. Electro-oxidation of H 2 and H 2/CO Mixtures on Pt-Based Gas-Diffusion Electrodes." *J. Electrochem. Soc.*, **146**, 4031 (1999).
16. M. Ciureanu, S. D. Mikhailenko, and S. Kaliaguine, "PEM fuel cells as membrane reactors: kinetic analysis by impedance spectroscopy." *Catal. Today*, **82**, 195 (2003).
17. A. G. Hombrados, L. González, M. A. Rubio, W. Agila, E. Villanueva, D. Guinea, E. Chinarro, B. Moreno, and J. R. Jurado, "Symmetrical electrode mode for PEMFC characterisation using impedance spectroscopy." *Journal of Power Sources*, **151**, 25 (2005).
18. M. Heinzmann, A. Weber, and E. Ivers-Tiffée, "Advanced impedance study of polymer electrolyte membrane single cells by means of distribution of relaxation times." *Journal of Power Sources*, **402**, 24 (2018).
19. K. C. Neyerlin, W. Gu, J. Jorne, and H. A. Gasteiger, "Determination of Catalyst Unique Parameters for the Oxygen Reduction Reaction in a PEMFC." *J. Electrochem. Soc.*, **153**, A1955 (2006).
20. A. Holewinski and S. Linic, "Elementary mechanisms in electrocatalysis: revisiting the ORR Tafel slope." *J. Electrochem. Soc.*, **159**, H864 (2012).
21. J. Huang, J. Zhang, and M. Eikerling, "Unifying theoretical framework for deciphering the oxygen reduction reaction on platinum." *Phys. Chem. Chem. Phys.*, **20**, 11776 (2018).
22. A. M. Gómez, "-Marín and E. A. Ticianelli. A reviewed vision of the oxygen reduction reaction mechanism on Pt-based catalysts." *Current Opinion in Electrochemistry*, **9**, 129 (2018).
23. B. P. Setzler and T. F. Fuller, "A physics-based impedance model of proton exchange membrane fuel cells exhibiting low-frequency inductive loops." *J. Electrochem. Soc.*, **162**, F519 (2015).
24. I. V. Zenyuk, "P. K. Das, and A. Z. Weber. Understanding Impacts of Catalyst-Layer Thickness on Fuel-Cell Performance via Mathematical Modeling." *J. Electrochem. Soc.*, **163**, F691 (2016).
25. Georg A. Futter, Pawel Gazdzicki, K. Andreas Friedrich, and Arnulf Latz, "and Thomas Jahnke. Physical modeling of polymer-electrolyte membrane fuel cells: Understanding water management and impedance spectra." *Journal of Power Sources*, **391**, 148 (2018).
26. A. Goshtasbi, P. García-Salaberri, J. Chen, K. Talukdar, and D. G. Sanchez, "and Tulga Ersal. Through-the-Membrane Transient Phenomena in PEM Fuel Cells: A Modeling Study." *J. Electrochem. Soc.*, **166**, F3154 (2019).
27. N. P. Subramanian, T. A. Greszler, J. Zhang, W. Gu, and R. Makharia, "Pt-oxide coverage-dependent oxygen reduction reaction (ORR) kinetics." *J. Electrochem. Soc.*, **159**, B531 (2012).
28. A. A. Kulikovsky and A. Physically, "Based Analytical Polarization Curve of a PEM Fuel Cell." *J. Electrochem. Soc.*, **161**, F263 (2014).
29. T. E. Springer, T. A. Zawodzinski, M. S. Wilson, and S. Gottesfeld, "Characterization of polymer electrolyte fuel cells using AC impedance spectroscopy." *J. Electrochem. Soc.*, **143**, 587 (1996).
30. D. Malevich, E. Halliop, B. A. Peppley, J. G. Pharoah, and K. Karan, "Investigation of Charge-Transfer and Mass-Transport Resistances in PEMFCs with Microporous Layer Using Electrochemical Impedance Spectroscopy." *J. Electrochem. Soc.*, **156**, B216 (2009).
31. S. Cruz-Manzo and R. Chen, "A generic electrical circuit for performance analysis of the fuel cell cathode catalyst layer through electrochemical impedance spectroscopy." *Journal of Electroanalytical Chemistry*, **694**, 45 (2013).
32. S. Cruz-Manzo and R. Chen, "An electrical circuit for performance analysis of polymer electrolyte fuel cell stacks using electrochemical impedance spectroscopy." *J. Electrochem. Soc.*, **160**, F1109 (2013).
33. N. Wagner, "Characterization of membrane electrode assemblies in polymer electrolyte fuel cells using ac impedance spectroscopy." *Journal of applied electrochemistry*, **32**, 859 (2002).
34. N. Wagner, T. Kaz, and K. A. Friedrich, "Investigation of electrode composition of polymer fuel cells by electrochemical impedance spectroscopy." *Electrochimica Acta*, **53**, 7475 (2008).
35. N. Wagner and K. A. Friedrich, "Application of Electrochemical Impedance Spectroscopy for Fuel Cell Characterization: PEFC and Oxygen Reduction Reaction in Alkaline Solution." *Fuel Cells*, **9**, 237 (2009).
36. M. Heinzmann, A. Weber, and E. Ivers-Tiffée, "Impedance modelling of porous electrode structures in polymer electrolyte membrane fuel cells." *Journal of Power Sources*, **444**, 227279 (2019).
37. A. A. Kulikovsky, "Analytical Models for PEM Fuel Cell Impedance." *Self-publishing, Eisma* (2018).
38. D. R. Baker, "D. A. Caulk, K. C. Neyerlin, and M. W. Murphy. Measurement of Oxygen Transport Resistance in PEM Fuel Cells by Limiting Current Methods." *J. Electrochem. Soc.*, **156**, B991 (2009).
39. D. A. Caulk and D. R. Baker, "Heat and Water Transport in Hydrophobic Diffusion Media of PEM Fuel Cells." *J. Electrochem. Soc.*, **157**, B1237 (2010).
40. M. Göbel et al., "Transient limiting current measurements for characterization of gas diffusion layers." *Journal of Power Sources*, **402**, 237 (2018).
41. Gregor S. Harzer, Jan N. Schwämmlein, Ana Marija Damjanović, Sourov Ghosh, and Hubert, "A. Gasteiger. Cathode Loading Impact on Voltage Cycling Induced PEMFC Degradation: A Voltage Loss Analysis." *J. Electrochem. Soc.*, **165**, F3118 (2018).
42. T. H. Wan, M. Saccoccio, C. Chen, and F. Ciucci, "Influence of the Discretization Methods on the Distribution of Relaxation Times Deconvolution: Implementing Radial Basis Functions with DRTtools." *Electrochimica Acta*, **184**, 483 (2015).
43. W. Vogel, L. Lundquist, P. Ross, and P. Stonehart, "Reaction pathways and poisonsII: The rate controlling step for electrochemical oxidation of hydrogen on Pt in acid and poisoning of the reaction by CO." *Electrochimica Acta*, **20**, 79 (1975).
44. K. Seto and A. Iannelli, "B.e Love, and J. Lipkowski. The influence of surface crystallography on the rate of hydrogen evolution at Pt electrodes." *Journal of electroanalytical chemistry and interfacial electrochemistry*, **226**, 351 (1987).
45. R. Notoya and A. Matsuda, "Determination of the rate of the discharge step of hydrogen ion on a hydrogen-platinum electrode in aqueous solutions by the galvanostatic transient method." *The Journal of Physical Chemistry*, **93**, 5521 (1989).
46. H. Kita, S. Ye, and Y. Gao, "Mass transfer effect in hydrogen evolution reaction on Pt single-crystal electrodes in acid solution." *Journal of Electroanalytical Chemistry*, **334**, 351 (1992).
47. N. M. Marković, B. N. Grgur, and P. N. Ross, "Temperature-dependent hydrogen electrochemistry on platinum low-index single-crystal surfaces in acid solutions." *The Journal of Physical Chemistry B*, **101**, 5405 (1997).
48. L. Giorgi, A. Pozio, C. Bracchini, R. Giorgi, and S. Turtu, "H2 and H2/CO oxidation mechanism on Pt/C, Ru/C and Pt-Ru/C electrocatalysts." *Journal of applied electrochemistry*, **31**, 325 (2001).
49. H. A. Gasteiger, J. E. Panels, and S. G. Yan, "Dependence of PEM fuel cell performance on catalyst loading." *Journal of Power Sources*, **127**, 162 (2004).
50. S. Chen and A. Kucernak, "Electrocatalysis under Conditions of High Mass Transport: Investigation of Hydrogen Oxidation on Single Submicron Pt Particles Supported on Carbon." *The Journal of Physical Chemistry B*, **108**, 13984 (2004).
51. K. C. Neyerlin, W. Gu, J. Jorne, A. Clark, and H. A. Gasteiger, "Cathode Catalyst Utilization for the ORR in a PEMFC." *J. Electrochem. Soc.*, **154**, B279 (2007).
52. K. C. Neyerlin, W. Gu, J. Jorne, and H. A. Gasteiger, "Study of the Exchange Current Density for the Hydrogen Oxidation and Evolution Reactions." *J. Electrochem. Soc.*, **154**, B631 (2007).
53. K. Wiezell, P. Gode, and G. Lindbergh, "Steady-State and EIS Investigations of Hydrogen Electrodes and Membranes in Polymer Electrolyte Fuel Cells." *J. Electrochem. Soc.*, **153**, A749 (2006).
54. N. Holmström, K. Wiezell, and G. Lindbergh, "Studying Low-Humidity Effects in PEFCs Using EIS: I. Experimental." *J. Electrochem. Soc.*, **159**, F369 (2012).
55. K. Wiezell, N. Holmström, and G. Lindbergh, "Studying low-humidity effects in PEFCs using EIS II. modeling." *J. Electrochem. Soc.*, **159**, F379 (2012).

56. J. Kim, "Characterization of CO tolerance of PEMFC by ac impedance spectroscopy." *Solid State Ionics*, **140**, 313 (2001).
57. M. Mathias, D. Baker, J. Zhang, Y. Liu, and W. Gu, "Frontiers in Application of Impedance Diagnostics to H2-Fed Polymer Electrolyte Fuel Cells." *ECS Trans.*, **13**, 129 (2008).
58. H. Xu, Y. Song, H. R. Kunz, and J. M. Fenton, "Effect of Elevated Temperature and Reduced Relative Humidity on ORR Kinetics for PEM Fuel Cells." *J. Electrochem. Soc.*, **152**, A1828 (2005).
59. H. Xu, H. R. Kunz, and J. M. Fenton, "Analysis of proton exchange membrane fuel cell polarization losses at elevated temperature 120C and reduced relative humidity." *Electrochimica Acta*, **52**, 3525 (2007).
60. K. C. Neyerlin, H. A. Gasteiger, C. K. Mittelsteadt, J. Jorne, and W. Gu, "Effect of Relative Humidity on Oxygen Reduction Kinetics in a PEMFC." *J. Electrochem. Soc.*, **152**, A1073 (2005).
61. Y. Liu, M. W. Murphy, D. R. Baker, W. Gu, C. Ji, J. Jorne, and H. A. Gasteiger, "Proton Conduction and Oxygen Reduction Kinetics in PEM Fuel Cell Cathodes: Effects of Ionomer-to-Carbon Ratio and Relative Humidity." *J. Electrochem. Soc.*, **156**, B970 (2009).
62. A. T. S. Freiberg, M. C. Tucker, and A. Z. Weber, "Polarization loss correction derived from hydrogen local-resistance measurement in low Pt-loaded polymer-electrolyte fuel cells." *Electrochemistry Communications*, **79**, 14 (2017).
63. D. R. Baker and D. A. Caulk, "Limiting Current as a Tool to Study Oxygen Transport in PEM Fuel Cells." *ECS Trans.*, **50**, 35 (2013).
64. C. Simon, D. Kartouzian, D. Mueller, F. Wilhelm, and H. A. Gasteiger, "Impact of microporous layer pore properties on liquid water transport in PEM fuel cells: carbon black type and perforation." *J. Electrochem. Soc.*, **164**, F1697 (2017).
65. O. E. Herrera, D. P. Wilkinson, and W. Mérida, "Anode and cathode overpotentials and temperature profiles in a PEMFC." *Journal of Power Sources*, **198**, 132 (2012).